CHALMERS

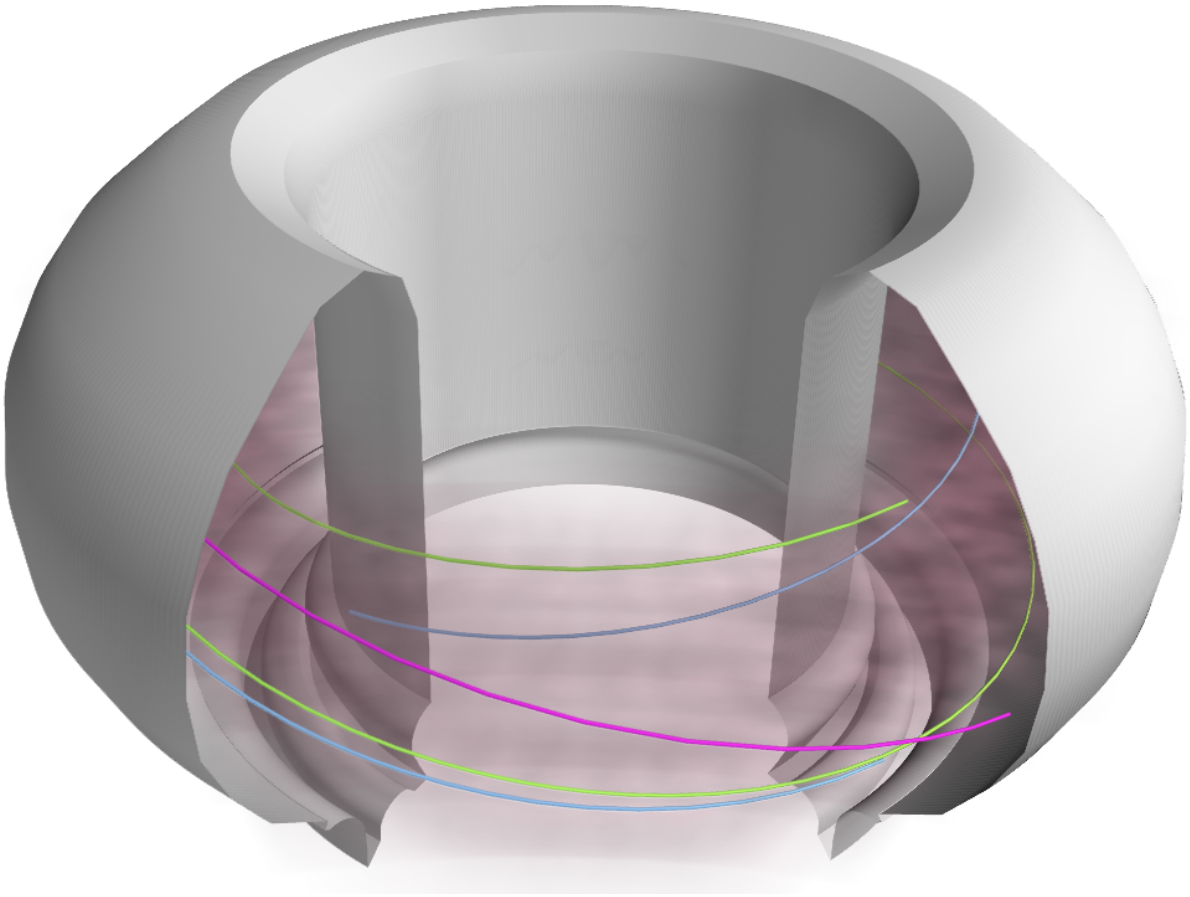

# Simulation of Charged Particle Orbits in Fusion Plasmas

Bachelor's thesis in Engineering Physics

MATHIAS HOPPE
AYLWIN IANTCHENKO
INGRID STRANDBERG

Department of Applied Physics
CHALMERS UNIVERSITY OF TECHNOLOGY
Göteborg, Sweden 2015

Bachelor's thesis in Engineering Physics

# Simulation of Charged Particle Orbits in Fusion Plasmas

Mathias Hoppe
Aylwin Iantchenko
Ingrid Strandberg

Department of Applied Physics
CHALMERS UNIVERSITY OF TECHNOLOGY
Göteborg, Sweden 2015

SIMULATION OF CHARGED PARTICLE ORBITS IN FUSION PLASMAS

Mathias Hoppe
Aylwin Iantchenko
Ingrid Strandberg



Bachelor's thesis TIFX02-15-41
Department of Applied Physics
Chalmers University of Technology
SE-412 96 Göteborg
Sweden
Telephone: +46 (0)31-772 1000

Cover:
A 3D model of the International Thermonuclear Experimental Reactor (ITER) with charged particle orbits, each of duration 15 $\mu$s, plotted in different colors. The orbits were calculated using the tools developed for this project.

Chalmers Reproservice
Göteborg, Sweden 2015

SIMULATION OF CHARGED PARTICLE ORBITS IN FUSION PLASMAS

Mathias Hoppe
Aylwin Iantchenko
Ingrid Strandberg
Department of Applied Physics
Chalmers University of Technology

# Abstract

When designing a fusion device, knowledge of the particle motion inside the fusion plasma is crucial. The charged plasma particles are confined inside the device using a strong magnetic field, which influences particle motion. Particle trajectories can therefore be obtained by numerically solving the equations of motion for a charged particle in the confining magnetic field.

With the simulation tool developed as a part of this project, charged particle orbits are studied. Especially, the properties of the so called banana and passing orbit topologies are studied and the observed results explained using theoretical models. We find expressions that approximately describe the width of the banana and passing orbits and the location of the banana orbit's mirror points.

The orbit dependence on mass, charge and energy is investigated and an expression for the particle's deviation from a field line is derived. Also, the cause for banana orbits forming is studied and their occurrence is shown to depend on how the particle's velocity vector is directed. Finally, the two computational methods used, where either the particle or its guiding-center is followed, are compared with respect to both energy conservation and computational time. The guiding-center approach is shown to greatly reduce computational cost.

# Sammandrag

När en fusionsanordning ska designas krävs kunskap om hur partiklarna som utgör fusionsplasmat rör sig. De laddade plasmapartiklarna hålls instängda i fusionsanordningen med hjälp av starka magnetfält som påverkar partiklarnas rörelse. Partikelbanorna kan därför beräknas genom att ställa upp och numeriskt lösa rörelsekvationerna för laddade partiklar i magnetfält.

Partikelbanor studeras med hjälp av det simuleringsverktyg som speciellt utvecklats för detta projekt. I synnerhet studeras egenskaperna hos så kallade banan- och övergångsbanor. Med hjälp av teoretiska modeller förklaras de gjorda observationerna och uttryck för bland annat banornas bredd samt läget för banan-banans spegelpunkter tas fram.

Banans beroende av massa, laddning och energi undersöks och ett uttryck för partikelns avvikelse från en fältlinje härleds. Även orsaken till att banan-banor uppstår studeras och deras uppkomst visar sig bero på hur partikelns hastighetsvektor är riktad. Slutligen jämförs de två beräkningsmetoderna som används, där antingen partikeln eller dess bancentra följs, med avseende på energikonservering och beräkningshastighet. Att följa bancentrat visar sig vara beräkningsmässigt effektivare.

# Acknowledgements

We would first like to thank our supervisors: Eero Hirvijoki, for tirelessly and with dedication teaching us the theory of the subject of this thesis, as well as pushing us to do our very best, and István Pusztai, for constantly giving insightful and enlightening comments, even when commitments outside of Gothenburg and Sweden kept him busy. Thank you both for always being at hand to give answers whenever we had questions.

We would also like to thank Professor Tünde Fülöp, for being so kind and making us feel very welcome into the electromagnetic field theory research group.

The Authors, Göteborg, May 2015

# Contents

*"You do not follow the path of a hummingbird by looking at every flap of its wings"*

Alain J. Brizard (paraphrased)

# 1 Introduction

Together with increasing electricity demands and climate change, the need for an environmentally friendly substitute to fossil fuel is necessary. One of the most promising long term candidates is nuclear fusion, which generates energy by fusing lighter nuclei into heavier ones. The energy released during fusion comes from the difference in the binding energies of the initial and final states. The goal of controlled fusion research is to extract this energy.

In order to induce these reactions, very high temperatures are needed. These processes occur naturally in stars, including our Sun, in which temperatures are of the order 10 million K [1]. In order to produce nuclear fusion on Earth however, temperatures of the order 100 million K are required [2]. This is because we use a different fusion reaction than the dominant processes in the Sun. Additionally, there is a tremendously high pressure in the core of the Sun which cannot be produced in fusion devices. As fuel used for fusion devices must be heated to extreme temperatures, a substantial problem becomes apparent: there are no materials capable of withstanding such high temperatures.

A star is held together by its own gravitational field. On Earth we provide confinement by using a property of the fusion fuel which arises at high temperatures. As the temperature rises in any material, atoms start to move faster. This movement gives rise to the different states of matter, such as solid, liquid and gaseous. At high enough temperatures atoms start colliding and cause electrons to be released, thus creating an ionized gas state called a plasma state. The property of being ionized makes the plasma susceptible to the effects of electric and magnetic fields.

Applying a straight magnetic field in a plasma will make the constituent charged particles move in a helical orbit around the magnetic field lines. This straight magnetic field is sufficient for containing charged particle motion that is perpendicular to the field lines, but if a particle has a velocity component parallel with the field lines, it will drift towards the front and back walls of the device. Having charged particles repeatedly collide with the device walls would cause severe damage, as well as lead to an unacceptably high rate of energy loss.

A better approach is instead to bend the magnetic field into a torus shape, so that particles are lead in a circular orbit inside the device. This is the approach taken today in fusion research and it is utilized in the most successful types of fusion devices: tokamaks [3] and stellarators [4]. There are several operational differences between these two kinds of devices, but the idea of a bent torus-shaped magnetic field is used in both. In this project, magnetic equilibrium data from the tokamak *International Thermonuclear Experimental Reactor* (ITER) will be used. A model of ITER can be seen in Fig. 1.

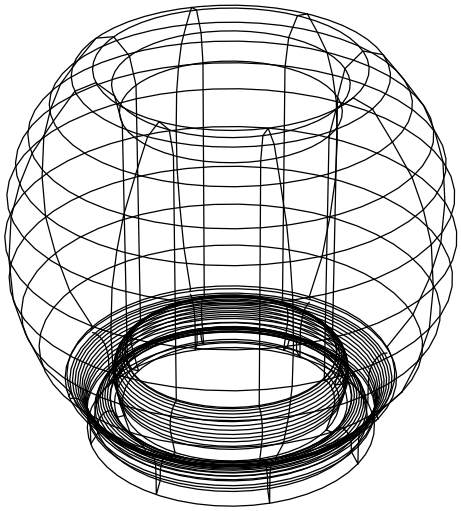

**Figure 1:** The outline of the inner walls of the International Thermonuclear Experimental Reactor.

The confinement of the fusion plasma comes with additional difficulties to those just mentioned. The hot plasma contains high energy free electrons and ions, so one of the difficulties is to trap the high energy particles in such a way that they deposit their energy inside the core of the plasma. This is of paramount importance in order to maintain the high temperature, and also to prevent highly energetic particles from hitting the device walls, and thus causing damage to them. Accordingly, the magnetic geometry has to be meticulously optimized for this to be done successfully. Because of this, knowledge of the particle motion inside the plasma is necessary when designing a fusion device. To achieve this, the equations of motion for a charged particle in a magnetic field need to be solved. This has been the main focus of the project.

## 1.1 Purpose

In this project, the trajectories of charged particles inside a tokamak fusion device will be simulated and studied. Simulations will be done using two different methods, except for when performance restrictions prevent the use of either of the methods. Observations made in the simulations will then be explained using theoretical models, and the two methods of simulation will be compared in terms of performance and agreement. Simulations will be performed by numerically solving the equations of motion applicable to the system, and in order to do this a specialized simulation tool must be developed.

## 1.2 Limitations

The goal is to follow collisionless, single particle orbits within a given static, inhomogeneous magnetic field. The collisionless description means neglecting the possibility of collision between particles. To take collisions into account stochastic methods are necessary, which is outside the scope of this project. We restrict the problem to deterministic (time-reversible) processes. For high energy particles collisionless theory is often well justified, since the collision frequency is proportional to $T^{-3/2}$, where $T$ is the kinetic energy of the particle [5]. The frequency of collisions is typically much lower than the frequency of particle transit in the device.

Time-varying fields will not be considered. This is because in real tokamaks the confining magnetic field varies slowly enough to be considered constant for our application. There are fluctuating fields as well due to turbulence and instabilities, but that is also outside the scope of the thesis.

In the plasma, each charged particle contributes to the electric and magnetic fields. If there are many particles they can significantly affect the fields. We will not consider this "feedback", which essentially means that only a small number of particles will be taken into account. When particle motion in real tokamak geometry is studied, we will focus on the effects of the magnetic field, excluding electric fields. Furthermore, particles with high enough energy that they require a relativistic description will not be covered. The exclusion of electric fields and relativistic particles is mainly due to that including these phenomena would make the calculations more complex, yet it would not add essentially to the understanding.

## 1.3 Method

In this project both analytical mechanics and numerical methods will be used to simulate and visualize the motion of charged particles in the inhomogeneous magnetic field of a tokamak device. Given the magnetic vector field, the initial position and velocity of the charged particle as well as its mass and charge, the particle's trajectory inside the reactor will be traced.

First, in Section 2, the theory for charged particle motion in electromagnetic fields will be reviewed. We will begin in Section 2.1 by solving the equations of motion in a simple, straight, homogeneous magnetic field. This gives the well-known result that the particle gyrates around a field line as it moves along it. After this, we solve for an inhomogeneous magnetic field, discovering particle drifts. Since the gyrations are not of interest on a larger scale, we wish to decouple the gyro-motion from the non-trivial guiding-center motion. Using methods of analytical mechanics in Section 2.2, a Lagrangian for the guiding-center and its following equations of motion are derived.

Because the resulting equations of motion cannot be solved analytically, a numerical ordinary differential equation (ODE) solver was written using the C programming language. In Section 3 the magnetic field data is described, the included algorithms are explained, and the overall program workflow is presented.

In Section 4, the simulation results found using the tool developed are presented. In Section 4.1, the trajectories for different kinds of particles are shown in figures. An analysis of the observed particle motion follows in Section 4.2. Finally, we compare the results obtained from calculations of the particle motion versus the guiding-center motion. The performance of the numerical solver in the two different cases is also compared. It becomes clear why the guiding-center approach is needed: it reduces the computational cost tremendously.

# 2 Analytical theory of particle motion

Since the plasma consists of a large number of charged particles such as electrons, hydrogen ions and alpha particles, each of these particles will be affected by a force from the electric and magnetic field. This force is the well-known *Lorentz force* and it takes the form

$$\boldsymbol{F} = q\left(\boldsymbol{E} + \boldsymbol{v} \times \boldsymbol{B}\right), \tag{1}$$

where $q$ is the particle charge, $\boldsymbol{E}$ the electric field, $\boldsymbol{v}$ the particle velocity and $\boldsymbol{B}$ the magnetic field.

Since the goal of this project is to study the motion of various charged particles within the fusion plasma, we make several assumptions that should not affect the qualitative conclusions drawn from the later analysis. First we assume that there are no other forces but the Lorentz force acting on the particles. This is valid since gravitational effects are clearly negligible due to the ratio $mg/qvB$ (which is a rough estimate of gravitational effects compared to magnetic effects) being of the order $10^{-10}$ at most, for an alpha particle.

To simplify the treatment of the problem, we neglect electric fields, though these can be added in a straightforward way if desired. The total force acting on a plasma particle is then

$$\boldsymbol{F} = q\boldsymbol{v} \times \boldsymbol{B}.$$

Using Newton's second law we can now write the equations of motion for a charged particle in a fusion plasma as

$$\begin{cases} \dot{\boldsymbol{v}} &= \frac{q}{m}\boldsymbol{v} \times \boldsymbol{B}, \\ \dot{\boldsymbol{r}} &= \boldsymbol{v}. \end{cases} \tag{2}$$

These equations will be solved analytically for special cases in the following two subsections. First, in Section 2.1.1, they are solved in a static, homogeneous magnetic field after which the resulting expressions for the particle motion is discussed. Then, in Section 2.1.2, the particle motion is studied in a more general, inhomogeneous magnetic field.

To decrease computational cost in numerical calculations, it is of interest to decouple the gyro-motion of the particle from its guiding-center motion. This is done using the *guiding-center transformation*, and in Section 2.2 the Lagrangian and its associated equations of motion for the guiding-center will be derived.

## 2.1 Particle Motion

We want to gain an understanding of the particle motion in strongly magnetized plasmas. The magnetic fields present in fusion devices are quite complicated and require numerical methods for tracing the charged particles, but starting out with a simple magnetic field will give us a qualitative understanding of what happens to the particle. We develop this step by step. The simplest possible set-up is a straight homogeneous field, which will be examined first.

### 2.1.1 Particle motion in a homogeneous magnetic field

For a particle in a straight static magnetic field, $\boldsymbol{B} = B\hat{\boldsymbol{x}}$, where $B$ is the magnetic field strength (which is assumed constant for now), the equations of motion (2) can

be written as

$$\dot{v}_x = 0, \tag{3}$$
$$\dot{v}_y = \frac{q}{m} v_z B, \tag{4}$$
$$\dot{v}_z = -\frac{q}{m} v_y B, \tag{5}$$
$$\dot{\boldsymbol{r}} = \boldsymbol{v}. \tag{6}$$

With the initial conditions $\boldsymbol{r}_0 = (x_0, y_0, z_0)$ and $\boldsymbol{v}_0 = (v_{x0}, v_{y0}, v_{z0})$ the first of these equations is easily solved to give

$$x(t) = v_{x0} t + x_0.$$

To solve for $y$ and $z$, we begin by differentiating both (4) and (5) with respect to time in order to get

$$\ddot{v}_y = \frac{q}{m} \dot{v}_z B,$$
$$\ddot{v}_z = -\frac{q}{m} \dot{v}_y B.$$

Substituting the expressions for $\dot{v}_y$ and $\dot{v}_z$ into these equations, defining $\Omega = |q|B/m$ and reordering the terms, gives us two second order differential equations of the familiar forms

$$\ddot{v}_y + \Omega^2 v_y = 0,$$
$$\ddot{v}_z + \Omega^2 v_z = 0.$$

These equations have periodic solutions that can be written as

$$v_y = \mathrm{Re}\left[ C e^{i\Omega t} \right], \tag{7}$$
$$v_z = \mathrm{Re}\left[ D e^{i\Omega t} \right], \tag{8}$$

where $C$ and $D$ are complex integration constants. Using Eq. (4) we get the relation between $C$ and $D$ as $C = i\,\mathrm{sgn}(q) D$, where $\mathrm{sgn}(q)$ denotes the sign of the charge $q$. This essentially means that $v_y$ and $v_z$ are offset from each other by a phase angle of $90°$, and allows us to determine $|C|$ by adding the squares of $v_y$ and $v_z$. If we define the perpendicular velocity to be $v_\perp \equiv (v_y^2 + v_z^2)^{1/2}$, we get

$$\big(v_y(t)\big)^2 + \big(v_z(t)\big)^2 = |C|^2(\cos^2 \Omega t + \sin^2 \Omega t) = v_\perp^2 \equiv \sqrt{v_{y0}^2 + v_{z0}^2},$$

where the last identity holds since $C$ is a constant. Note that this means $v_\perp$ will remain constant. Since $v_x$ is also constant, the kinetic energy is constant: the magnetic field does no work on the particle.

Because $C$ is a *complex* constant, the above is not enough to fully determine its value. We can however write $C$ in polar form, offset by some phase angle $\phi$, as $C = v_\perp e^{i\phi}$. Dividing $v_y(0) = v_{y0}$ by $v_z(0) = v_{z0}$ then gives

$$\phi = -\,\mathrm{sgn}(q) \arctan\left( \frac{v_{z0}}{v_{y0}} \right).$$

Finally, by integrating (7) and (8) in time and using the initial conditions $y(0) = y_0$ and $z(0) = z_0$ we arrive at the expressions determining the particle position in the $y$-$z$ plane,

$$\begin{aligned} y(t) &= y_{\text{gc}} - \text{Re}\left[i\frac{v_\perp}{\Omega}e^{i(\Omega t+\phi)}\right], \\ z(t) &= z_{\text{gc}} + \text{sgn}(q)\,\text{Re}\left[\frac{v_\perp}{\Omega}e^{i(\Omega t+\phi)}\right], \end{aligned} \tag{9}$$

where $y_{\text{gc}} = y_0 + (v_\perp/\Omega)\,\text{Re}(e^{i\phi})$ and $z_{\text{gc}} = z_0 - (v_\perp/\Omega)\,\text{sgn}(q)\,\text{Re}(e^{i\phi})$. These equations carry some very useful information. The first thing we notice is that the motion of the particle in the magnetic field is in the shape of a helix around the magnetic field line, illustrated in Fig. 2. As we will see, the qualitative behavior remains similar even for more complicated magnetic fields. It also motivates the important guiding-center transformation which will be discussed later.

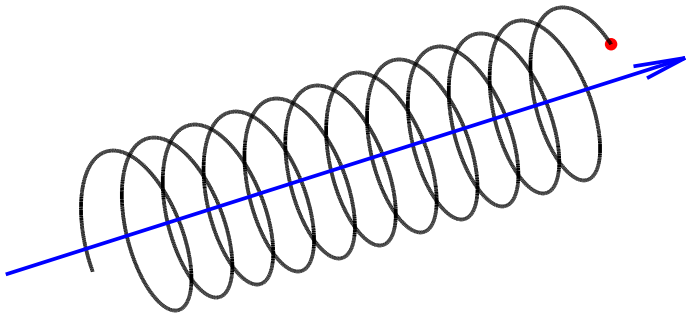

**Figure 2:** The motion of an electron in a straight magnetic field. A magnetic field line has been visualized for reference.

From the expressions above we also notice the importance of the three quantities $y_{\text{gc}}$, $z_{\text{gc}}$ and $v_\perp/\Omega \equiv \rho$. The first two denote the position of the center of the gyromotion made by the particle. This point, $(y_{\text{gc}}, z_{\text{gc}})$, is often referred to as the *guiding-center* or *gyro-center*. The third quantity is the gyration radius, commonly referred to as the *Larmor radius* and denoted $\rho$, which determines the size of the helical orbit in the plane perpendicular to the field line. With these quantities it is useful to define

$$\boldsymbol{x} = \boldsymbol{X} + \boldsymbol{\rho}, \tag{10}$$

where $\boldsymbol{x}$ is the particle position, $\boldsymbol{X}$ is the guiding-center and $\boldsymbol{\rho}$ is the gyro-radius vector. This will be used in following sections, starting with 2.1.2.

### 2.1.2 Particle drifts in inhomogeneous magnetic fields

From the theory of straight magnetic fields above, we can easily conclude that a particle with even a very small velocity component parallel to the magnetic field would cause the particle to follow the field line until some physical boundary stops the particle. Therefore, in order to contain the particle for a sufficiently long time, a device of considerable length would be required. This is obviously not practical,

and so instead the device is bent into a torus (see Fig. 1). This bending of the device however, also requires the magnetic field to be curved along with it, making the forces acting on the particle different. When the magnetic field is curved, its strength should have a spatial variation due to its divergence-free nature, which will cause yet another force acting on the particle.

In this project, knowledge about particle drifts will be needed later on when particle orbits are analyzed, though we will mostly need some basic results of this theory. Because of this, the theory derived in this section is only derived briefly, with several details left out. A more exhaustive analysis of particle drifts can be found for example in the book by Chen (1984) [6].

### Constant force

In order to simplify later calculations, let us first study what happens to the particle when we apply a general force $\boldsymbol{F} = F_x\hat{\boldsymbol{x}} + F_y\hat{\boldsymbol{y}} + F_z\hat{\boldsymbol{z}}$. Keeping the straight magnetic field $\boldsymbol{B} = B\hat{\boldsymbol{x}}$ for now, we add the force $\boldsymbol{F}$ to the equations of motion (2),

$$\begin{aligned}
\dot{v}_x &= \frac{1}{m}F_x, \\
\dot{v}_y &= \frac{q}{m}v_z B + \frac{1}{m}F_y, \\
\dot{v}_z &= -\frac{q}{m}v_y B + \frac{1}{m}F_z.
\end{aligned}$$

By requiring $\boldsymbol{F}$ to be constant, we can solve these equations rather easily in the same way we solved (2) earlier. This yields the solutions

$$\begin{aligned}
v_x &= \frac{F_x}{m}t + v_{x0}, \\
v_y &= \mathrm{Re}\left[v_\perp e^{i\Omega t+\phi}\right] + \frac{F_z}{qB}, \\
v_z &= \mathrm{sgn(q)Re}\left[iv_\perp e^{i\Omega t+\phi}\right] - \frac{F_y}{qB}.
\end{aligned}$$

The motion in the $x$-direction (parallel to the magnetic field lines) has now become accelerating, just as expected from Newtons second law. This component will not be of great concern to us, as it is along the magnetic field line, and so will not cause the particle to deviate from the field lines. However, we also found that in the $y$- and $z$-directions a velocity perpendicular to the field lines is induced. It is interesting to note that this velocity causes the particle's guiding-center to gradually move across the magnetic field, or in other words, causes it to drift. The velocity $\boldsymbol{v}_{gc} = (1/qB)(F_z\hat{\boldsymbol{y}} - F_y\hat{\boldsymbol{z}})$ is therefore referred to as a *drift velocity*.

It is possible to obtain a general formula for the drift velocity, $\boldsymbol{v}_{gc}$, which holds also for general forces $\boldsymbol{F}$ and magnetic fields $\boldsymbol{B} = B(x, y, z, t)\hat{\boldsymbol{b}}$. To obtain this formula, we start from the vector form of the equations of motion,

$$m\dot{\boldsymbol{v}} = q\boldsymbol{v} \times \boldsymbol{B} + \boldsymbol{F}.$$

Since the $m\dot{\boldsymbol{v}}$ term only gives the gyro-motion, which we already know about, we can omit it. We form the vector product of the resulting equation with $\boldsymbol{B}$ and rewrite

the expression a bit,

$$\begin{aligned} q(\boldsymbol{v}\times\boldsymbol{B})\times\boldsymbol{B}+\boldsymbol{F}\times\boldsymbol{B}=0 \quad &\Longleftrightarrow \\ q(B^2\boldsymbol{v}-v_{||}B^2\hat{\boldsymbol{b}}) &= \boldsymbol{F}\times\boldsymbol{B}, \end{aligned} \tag{11}$$

where $v_{||}=\boldsymbol{v}\cdot\hat{\boldsymbol{b}}$. We assume now that the velocity $\boldsymbol{v}$ can be decomposed into one part parallel with the magnetic field, $\boldsymbol{v}_{||}=v_{||}\hat{\boldsymbol{b}}$, and one part perpendicular to the magnetic field, $\boldsymbol{v}_F$. The left-hand side of Eq. (11) then simply becomes $q\boldsymbol{v}_F$, and we can write an expression for the drift velocity,

$$\boldsymbol{v}_F=\frac{\boldsymbol{F}\times\boldsymbol{B}}{qB^2}. \tag{12}$$

As mentioned above, this formula is general and applies to any force $\boldsymbol{F}$ and magnetic field $\boldsymbol{B}$.

### $\nabla B$ drift

Let us study the magnetic field $\boldsymbol{B}=B(y,z)\hat{\boldsymbol{x}}$, which only varies in the $\hat{\boldsymbol{y}}$ and $\hat{\boldsymbol{z}}$ directions, so that $\nabla B\perp\boldsymbol{B}$. It is not possible to analytically find an exact solution for $\boldsymbol{B}$ of a general form. However, since the Larmor radius is much smaller than the typical length scale over which $\boldsymbol{B}$ varies, $\boldsymbol{B}$ can be expanded in a Taylor series around the particle orbit's guiding-center, to get an approximate expression for the drift velocity. Denote the magnetic field scale length $L_B=B/|\nabla B|$. The condition is then $\rho\ll L_B$, which is well satisfied in fusion devices for thermal particles. Since we are only interested in the drift velocity here, the velocity component in the $x$ direction will be ignored.

The expansion for our magnetic field around the guiding-center is

$$\boldsymbol{B}=\left[B(y_{gc},z_{gc})+(y-y_{gc})\frac{\partial B}{\partial y}+(z-z_{gc})\frac{\partial B}{\partial z}+\mathcal{O}(\rho^2)\right]\hat{\boldsymbol{x}}.$$

Using Equations (4) and (5), and the expansion above to first order, we get the new equations

$$\begin{aligned} m\dot{v}_y=F_y&=qv_z\left[B(y_{gc})+(y-y_{gc})\frac{\partial B}{\partial y}+(z-z_{gc})\frac{\partial B}{\partial z}\right], \\ m\dot{v}_z=F_z&=-qv_y\left[B(y_{gc})+(y-y_{gc})\frac{\partial B}{\partial y}+(z-z_{gc})\frac{\partial B}{\partial z}\right]. \end{aligned}$$

Since we are only interested in the drifts of the guiding-center, not the actual gyrations, we average the force over a gyration period. From Eq. (9) we easily find the gyration period time to be $\tau=2\pi/\Omega$. Denoting the average force as $\langle F\rangle$, and substituting the expressions for $v_y$ and $v_z$ from (7) and (8) to get an approximate

expression, we find

$$\langle F_y \rangle = \frac{1}{\tau}\int_0^\tau -|q|v_\perp \sin(\Omega t+\phi)\Bigg[B(y_{gc}) + \rho\sin(\Omega t+\phi)\frac{\partial B}{\partial y} + \\ + \rho\,\mathrm{sgn}(q)\cos(\Omega t+\phi)\frac{\partial B}{\partial z}\Bigg]dt = -\frac{|q|v_\perp\rho}{2}\frac{\partial B}{\partial y},$$

$$\langle F_z \rangle = \frac{1}{\tau}\int_0^\tau -qv_\perp \cos(\Omega t+\phi)\Bigg[B(y_{gc}) + \rho\sin(\Omega t+\phi)\frac{\partial B}{\partial y} + \\ + \rho\,\mathrm{sgn}(q)\cos(\Omega t+\phi)\frac{\partial B}{\partial z}\Bigg]dt = -\frac{|q|v_\perp\rho}{2}\frac{\partial B}{\partial z}.$$

We can now set the force $\boldsymbol{F}_{\nabla B} = (0, \langle F_y\rangle, \langle F_z\rangle)$ and use Eq. (12) to find an expression for the drift velocity. Noting that the choice for the orientation of $\boldsymbol{B}$ was entirely arbitrary, as long as the gradient is perpendicular to it, we can find the general expression for the drift velocity due to a perpendicular gradient

$$\boldsymbol{v}_{\nabla B} = \frac{mv_\perp^2}{2qB^2}(\hat{\boldsymbol{b}} \times \nabla B). \tag{13}$$

This equation predicts that the guiding-center drift velocity of the particle will be in a direction perpendicular to both $\hat{\boldsymbol{b}}$ and $\nabla B$.

A physical picture for the $\nabla B$ drift is shown in Fig. 3, and follows from the fact that the local radius of curvature of the gyro-orbit is smaller on the side of the orbit with a larger magnetic field, and correspondingly, the radius is larger on the side with the smaller magnetic field. If the trajectories are calculated and plotted for such orbits, a net drift perpendicular to both $\hat{\boldsymbol{b}}$ and $\nabla B$ can be seen [5].

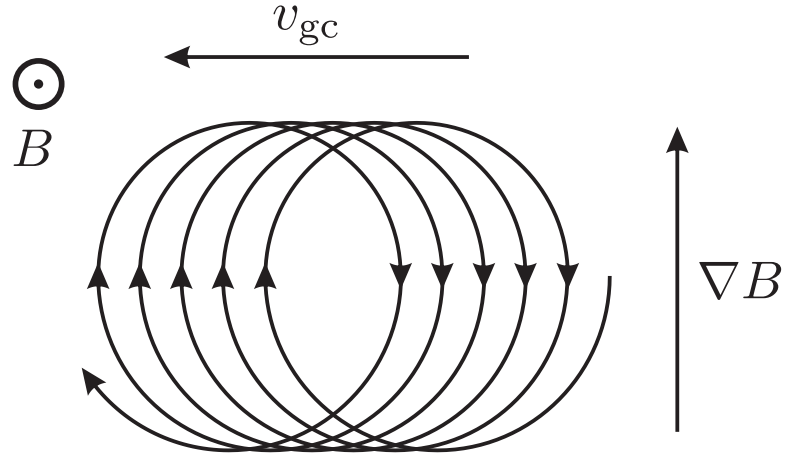


**Figure 3:** Ion $\nabla B$ drift motion. The gradient is directed upwards, and the dot indicates that the magnetic field points outwards from the page. The resulting guiding-center drift $\boldsymbol{v}_{\mathrm{gc}}$ is leftward, perpendicular to both $\nabla B$ and $\boldsymbol{B}$.

### Curvature drift

Apart from the $\nabla B$ drift, drift motion due to the curved geometry of the field will also arise. This drift motion comes from the centripetal force acting on the particle

which can be written as

$$\boldsymbol{F}_{\mathrm{c}} = \frac{mv_{\parallel}^2}{R_{\mathrm{c}}}\hat{\boldsymbol{r}} = \frac{mv_{\parallel}^2 \boldsymbol{R}_{\mathbf{c}}}{R_{\mathrm{c}}^2}, \tag{14}$$

where $R_{\mathrm{c}}$ is the local curvature radius of the field. We also assume the field strength $B$ to be locally constant. Inserting (14) into (12) gives us the curvature drift velocity

$$\boldsymbol{v}_c = \frac{\boldsymbol{F} \times \boldsymbol{B}}{qB^2} = \frac{mv_{\parallel}^2}{qB^2}\frac{\boldsymbol{R}_{\mathbf{c}} \times \boldsymbol{B}}{R_{\mathrm{c}}^2}.$$

The radius of curvature can be written as $\boldsymbol{R}_{\mathbf{c}}/R_{\mathrm{c}}^2 = -(\hat{\boldsymbol{b}} \cdot \nabla)\hat{\boldsymbol{b}}$. Define $\hat{\boldsymbol{b}} \cdot \nabla = \nabla_{\parallel}$, the gradient along $\hat{\boldsymbol{b}}$. The curvature drift velocity can now be expressed as

$$\boldsymbol{v}_c = \frac{mv_{\parallel}^2}{qB}\hat{\boldsymbol{b}} \times \nabla_{\parallel}\hat{\boldsymbol{b}}. \tag{15}$$

In this form it is evident that the curvature drift is caused by parallel gradients in $\hat{\boldsymbol{b}}$ (with a gradient scale length $L \gg \rho$).

## 2.2 Guiding-center motion

In the previous sections the particle motion has been described, showing the small gyration together with the overall guiding-center motion. However, in some situations it is desirable to focus only on the average displacement of the particle, neglecting the gyration. It is thus of interest to find how to separate these two different components of the motion, and only solve for the guiding-center motion. Because we are interested in how the particle moves on a much larger time scale than the gyrofrequency, and a much larger length scale than the Larmor radius, a Lagrangian for the guiding-center can be developed, from which the new equations of motion can be found.

### 2.2.1 Derivation of the guiding-center Lagrangian

The regular Lagrangian for a charged particle is

$$L = T - U = \frac{1}{2}m\boldsymbol{v}^2 - q\phi + q\boldsymbol{v} \cdot \boldsymbol{A}. \tag{16}$$

For a complete derivation of this Lagrangian, see Appendix A. The idea is now to derive a Lagrangian for which the gyro-motion is separated from the guiding-center motion. This will be done on the basis of slowly varying fields and a small Larmor radius. For a more thorough derivation we refer too the papers by Cary & Brizard (2009) [7] and Littlejohn (1983) [8]. The derivation follows the steps done in both of these papers, with some smaller modifications.

The Lagrangian we have right now is the same as that shown in Eq. (16), except we do not keep the electric potential term. It can be rewritten as

$$L = [q\boldsymbol{A} + m\boldsymbol{v}] \cdot \dot{\boldsymbol{x}} - \frac{1}{2}mv^2, \tag{17}$$

where $v = |\boldsymbol{v}|$. We want to find coordinates that transform the Lagrangian into the desired form. As introduced in Eq. (10), let the particle position be

$$\boldsymbol{x} = \boldsymbol{X} + \boldsymbol{\rho},$$

where $\boldsymbol{X}$ is the guiding-center position and $\boldsymbol{\rho}$ the Larmor vector. This has the total time derivative

$$\dot{\boldsymbol{x}} = \dot{\boldsymbol{X}} + \dot{\boldsymbol{\rho}}.$$

Let us now insert the new coordinates into our Lagrangian (17). Also, expand $\boldsymbol{A}(\boldsymbol{x})$ in a Taylor series around the guiding-center position $\boldsymbol{X}$.

$$\begin{aligned} L &= q[\boldsymbol{A} + \boldsymbol{\rho}\cdot\nabla\boldsymbol{A} + \mathcal{O}(\rho^2)]\cdot(\dot{\boldsymbol{X}} + \dot{\boldsymbol{\rho}}) + m\boldsymbol{v}\cdot(\dot{\boldsymbol{X}} + \dot{\boldsymbol{\rho}})\frac{1}{2}mv^2 = \\ &= q\boldsymbol{A}\cdot\dot{\boldsymbol{X}} + q\boldsymbol{A}\cdot\dot{\boldsymbol{\rho}} + q\boldsymbol{\rho}\cdot\nabla\boldsymbol{A}\cdot\dot{\boldsymbol{X}} + q\boldsymbol{\rho}\cdot\nabla\boldsymbol{A}\cdot\dot{\boldsymbol{\rho}} + m\boldsymbol{v}\cdot(\dot{\boldsymbol{X}} + \dot{\boldsymbol{\rho}})\frac{1}{2}mv^2 + \mathcal{O}(\rho^2). \end{aligned} \tag{18}$$

Note that the vector potential $\boldsymbol{A}$ is now evaluated at the guiding-center position, that is $\boldsymbol{A} = \boldsymbol{A}(\boldsymbol{X})$. Moving onwards, we will use the identities

$$\begin{aligned} \nabla\boldsymbol{A}\cdot\dot{\boldsymbol{X}} &= \dot{\boldsymbol{X}}\times\boldsymbol{B} + \dot{\boldsymbol{X}}\cdot\nabla\boldsymbol{A}, \\ \boldsymbol{A}\cdot\dot{\boldsymbol{\rho}} &= \frac{\mathrm{d}}{\mathrm{d}t}(\boldsymbol{A}\cdot\boldsymbol{\rho}) - \dot{\boldsymbol{X}}\cdot\nabla\boldsymbol{A}\cdot\boldsymbol{\rho}, \\ \boldsymbol{\rho}\cdot\nabla\boldsymbol{A}\cdot\dot{\boldsymbol{\rho}} &= \frac{1}{2}(\boldsymbol{\rho}\times\dot{\boldsymbol{\rho}}\cdot\boldsymbol{B}) + \frac{1}{2}\frac{\mathrm{d}}{\mathrm{d}t}(\boldsymbol{\rho}\cdot\nabla\boldsymbol{A}\cdot\dot{\boldsymbol{\rho}}) - \underbrace{\frac{1}{2}\boldsymbol{\rho}\cdot(\dot{\boldsymbol{X}}\cdot\nabla\nabla\boldsymbol{A})\cdot\boldsymbol{\rho}}_{\mathcal{O}(\rho^2)}. \end{aligned} \tag{19}$$

When substituting Equations (19) into the Lagrangian (18), one term will be canceled. To continue, we will use the gauge invariance of the Lagrangian, namely that the gauge transformation

$$L \to L + \frac{dF}{dt},$$

will not affect the equations of motion. A proof of this statement is given in Appendix B. This means that the two total time derivatives from (19) can be removed. We are then left with

$$L = q\boldsymbol{A}\cdot\dot{\boldsymbol{X}} + q\boldsymbol{\rho}\cdot(\dot{\boldsymbol{X}}\times\boldsymbol{B}) + \frac{q}{2}(\boldsymbol{\rho}\times\dot{\boldsymbol{\rho}}\cdot\boldsymbol{B}) + m\boldsymbol{v}\cdot(\dot{\boldsymbol{X}} + \dot{\boldsymbol{\rho}}) - \frac{1}{2}mv^2 + \mathcal{O}(\rho^2). \tag{20}$$

We continue by decomposing the velocity $\boldsymbol{v}$ into

$$\boldsymbol{v} = v_\parallel\hat{\boldsymbol{b}} + v_\perp\hat{\boldsymbol{c}}, \tag{21}$$

where the unit vector $\hat{\boldsymbol{b}}$ is in the direction of the magnetic field lines. The perpendicular unit vector $\hat{\boldsymbol{c}}$ is rotating with the angular velocity $\dot{\zeta} = \Omega$. The vector directions are illustrated in Fig. 4. There is also a unit vector $\hat{\boldsymbol{a}}$, $\hat{\boldsymbol{a}} = \hat{\boldsymbol{b}}\times\hat{\boldsymbol{c}}$ in the gyro-vector direction. The gyro-angle is denoted by $\zeta$. Expressions for $\hat{\boldsymbol{a}}$ and $\hat{\boldsymbol{c}}$ in terms of the gyro-angle $\zeta$ and a pair of fixed-frame, orthogonal unit vectors $\hat{\boldsymbol{e}}_1$ and $\hat{\boldsymbol{e}}_2$ satisfying $\hat{\boldsymbol{b}} = \hat{\boldsymbol{e}}_1\times\hat{\boldsymbol{e}}_2$ is shown in Eq. (22).

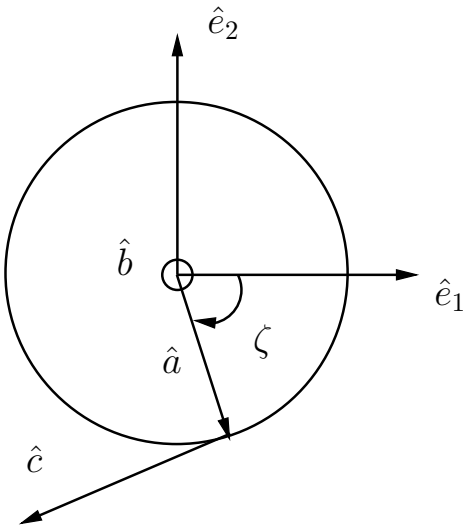


**Figure 4:** Coordinate unit vectors. A fixed frame is composed by $\hat{\boldsymbol{e}}_1$ and $\hat{\boldsymbol{e}}_2$. The vector $\hat{\boldsymbol{b}}$ is pointing in the direction of the magnetic field lines. The vector $\hat{\boldsymbol{c}}$ is rotating with the angular velocity $\dot{\zeta} = \Omega$. The vector $\hat{\boldsymbol{a}} = \hat{\boldsymbol{b}} \times \hat{\boldsymbol{c}}$ is pointing in the gyrovector direction.

$$\begin{aligned} \hat{\boldsymbol{a}} &= \cos(\zeta)\hat{\boldsymbol{e}}_1 - \sin(\zeta)\hat{\boldsymbol{e}}_2, \\ \hat{\boldsymbol{c}} &= -\sin(\zeta)\hat{\boldsymbol{e}}_1 - \cos(\zeta)\hat{\boldsymbol{e}}_2. \end{aligned} \tag{22}$$

We also note

$$\begin{aligned} \boldsymbol{\rho} &= \frac{v_\perp}{\Omega}\hat{\boldsymbol{a}}, \\ \dot{\boldsymbol{\rho}} &= \frac{d}{dt}\left(\frac{v_\perp}{\Omega}\hat{\boldsymbol{a}}\right) = \frac{v_\perp}{\Omega}\frac{d}{dt}(\hat{\boldsymbol{a}}) = \frac{v_\perp}{\Omega}\dot{\zeta}\hat{\boldsymbol{c}}. \end{aligned} \tag{23}$$

Insert (21) and (23) into the Lagrangian (20). Using the triple product rule and perpendicularity between vectors, after a few algebraic manipulations, we find the following Lagrangian:

$$L = \left[q\boldsymbol{A} + mv_\parallel\hat{\boldsymbol{b}}\right] \cdot \dot{\boldsymbol{X}} + \frac{m^2v_\perp^2}{2qB}\dot{\zeta} - \frac{1}{2}mv^2.$$

Furthermore, let $J = m^2v_\perp^2/2qB$ and note that $mv^2/2 = mv_\parallel^2/2 + \mu B$, where $\mu = mv_\perp^2/2B$ is the magnetic moment. The final Lagrangian becomes

$$L_{\mathrm{gc}}(\boldsymbol{X}, v_\parallel, \mu, \zeta; t) = \left[q\boldsymbol{A} + mv_\parallel\hat{\boldsymbol{b}}\right] \cdot \dot{\boldsymbol{X}} + J\dot{\zeta} - \frac{m}{2}v_\parallel^2 - \mu B. \tag{24}$$

Notice that we have carried out a transformation from the Lagrangian depending on the phase space coordinates $(\boldsymbol{x}, \boldsymbol{v}; t)$ to the guiding-center Lagrangian depending on the new coordinates $(\boldsymbol{X}, v_\parallel, \mu, \zeta; t)$.

As we can see, the guiding-center Lagrangian does not contain the coordinate $\zeta$, since it is a cyclic coordinate. From here it follows that $\partial L_{\mathrm{gc}}/\partial\dot{\zeta}$ is a constant of motion [9]. Evaluating this derivative gives

$$\frac{\partial L_{\mathrm{gc}}}{\partial\dot{\zeta}} = J = \frac{m}{q}\mu, \tag{25}$$

thus the magnetic moment can be regarded as a constant of motion for the guiding-center. Keep in mind that $\mu$ is really an adiabatic invariant, so it is only a constant of motion for the particle to first order approximation. A more in-depth look on this together with another derivation of the invariance of $\mu$ can be found in Appendix C.

The kinetic energy of the guiding-center motion is conserved in this case. This is due to the lack of an electric field. An energy gain is otherwise expected from work done by the electric field on the guiding-center. Including a time dependence of the magnetic field also adds to the energy. More details and calculations of this can be found in Northrop (1963) [10].

### 2.2.2 Derivation of the guiding-center equations of motion

The equations of motion are obtained from the Lagrangian (24) by applying the Euler-Lagrange equations for each of the phase-space coordinates $\boldsymbol{X}, v_\parallel, \mu$ and $\zeta$. Starting with $\zeta$ we get that

$$\frac{\partial L_{\text{gc}}}{\partial \dot{\zeta}} = \frac{m}{q}\mu, \quad \frac{\partial L_{\text{gc}}}{\partial \zeta} = 0,$$

and thus the equation of motion associated with $\zeta$ becomes

$$\frac{\mathrm{d}}{\mathrm{d}t}\left(\frac{\partial L_{\text{gc}}}{\partial \dot{\zeta}}\right) - \frac{\partial L_{\text{gc}}}{\partial \zeta} = 0 \implies \dot{\mu} = 0,$$

which indicates that $\mu$ is constant as stated earlier.

Moving on to the next parameter, $\mu$, we get that

$$\frac{\partial L_{\text{gc}}}{\partial \dot{\mu}} = 0, \quad \frac{\partial L_{\text{gc}}}{\partial \mu} = \frac{m}{q}\dot{\zeta} - B,$$

so the equation of motion associated with $\mu$ is

$$\dot{\zeta} = \frac{qB}{m} = \Omega.$$

Next, the derivatives of $L_{\text{gc}}$ with respect to $v_\parallel$ and $\dot{v_\parallel}$ are

$$\frac{\partial L_{\text{gc}}}{\partial \dot{v_\parallel}} = 0, \quad \frac{\partial L_{\text{gc}}}{\partial v_\parallel} = m\hat{\boldsymbol{b}} \cdot \dot{\boldsymbol{X}} - mv_\parallel,$$

and from the Euler-Lagrange equations we find

$$v_\parallel = \hat{\boldsymbol{b}} \cdot \dot{\boldsymbol{X}},$$

which states that $v_\parallel$ is the parallel velocity as was mentioned at the beginning.

We continue now with the derivation of the equation of motion for $\boldsymbol{X}$. We begin with the first partial derivative which gives

$$\begin{aligned}\frac{\partial L_{\text{gc}}}{\partial \boldsymbol{X}} &= q\nabla(\boldsymbol{A} \cdot \dot{\boldsymbol{X}}) + mv_\parallel \nabla(\hat{\boldsymbol{b}} \cdot \dot{\boldsymbol{X}}) - \mu \nabla B = \\ &= \dot{\boldsymbol{X}} \times \left[q\boldsymbol{B} + mv_\parallel(\nabla \times \hat{\boldsymbol{b}})\right] + \dot{\boldsymbol{X}} \cdot \nabla\big(q\boldsymbol{A} + mv_\parallel \hat{\boldsymbol{b}}\big) - \mu \nabla B,\end{aligned}$$

where we used the vector identity

$$\nabla\big(\boldsymbol{A}\cdot\dot{\boldsymbol{X}}\big)=\big(\boldsymbol{A}\cdot\nabla\big)\dot{\boldsymbol{X}}+\big(\dot{\boldsymbol{X}}\cdot\nabla\big)\boldsymbol{A}+\dot{\boldsymbol{X}}\times\big(\nabla\times\boldsymbol{A}\big)+\boldsymbol{A}\times\big(\nabla\times\dot{\boldsymbol{X}}\big),$$

and the fact that the operator $\nabla$ acting on $\dot{\boldsymbol{X}}$ is zero because $\dot{\boldsymbol{X}}$ is not explicitly position dependent. The next derivative is

$$\frac{\partial L_{\mathrm{gc}}}{\partial\dot{\boldsymbol{X}}}=q\boldsymbol{A}+mv_{\parallel}\hat{\boldsymbol{b}},$$

thus

$$\frac{\mathrm{d}}{\mathrm{d}t}\left(\frac{\partial L_{\mathrm{gc}}}{\partial\dot{\boldsymbol{X}}}\right)=q\nabla\boldsymbol{A}\cdot\dot{\boldsymbol{X}}+m\dot{v}_{\parallel}\hat{\boldsymbol{b}}+mv_{\parallel}\nabla\hat{\boldsymbol{b}}\cdot\dot{\boldsymbol{X}}.$$

Using the Euler-Lagrange equations

$$\frac{\mathrm{d}}{\mathrm{d}t}\frac{\partial L_{\mathrm{gc}}}{\partial\dot{\boldsymbol{X}}}=\frac{\partial L_{\mathrm{gc}}}{\partial\boldsymbol{X}},$$

we get the equations of motion

$$m\dot{v}_{\parallel}\hat{\boldsymbol{b}}=\dot{\boldsymbol{X}}\times\big[q\boldsymbol{B}+mv_{\parallel}(\nabla\times\hat{\boldsymbol{b}})\big]-\mu\nabla B.$$

We have now arrived at the following equations of motion:

$$\begin{aligned}\dot{\mu}=0,\qquad\dot{\zeta}=\Omega,\qquad v_{\parallel}=\hat{\boldsymbol{b}}\cdot\dot{\boldsymbol{X}},\\ m\dot{v}_{\parallel}\hat{\boldsymbol{b}}=\dot{\boldsymbol{X}}\times\big[q\boldsymbol{B}+mv_{\parallel}(\nabla\times\hat{\boldsymbol{b}})\big]-\mu\nabla B.\end{aligned}\tag{26}$$

Let us now manipulate the last one of these. By defining the effective magnetic field

$$\boldsymbol{B}^{*}=\nabla\times\left(\boldsymbol{A}+\frac{mv_{\parallel}}{q}\hat{\boldsymbol{b}}\right)=\boldsymbol{B}+\nabla\times\frac{mv_{\parallel}}{q}\hat{\boldsymbol{b}},\tag{27}$$

the last equation of Eq. (26) can be rewritten as

$$m\dot{v}_{\parallel}\hat{\boldsymbol{b}}=-\mu\nabla B+q\dot{\boldsymbol{X}}\times\boldsymbol{B}^{*}.\tag{28}$$

It is possible to solve Eq. (28) in terms of $\dot{\boldsymbol{X}}$ by doing a cross product of each term with $\hat{\boldsymbol{b}}$. Using $v_{\parallel}=\hat{\boldsymbol{b}}\cdot\dot{\boldsymbol{X}}$ we get

$$\dot{\boldsymbol{X}}=v_{\parallel}\frac{\boldsymbol{B}^{*}}{B_{||}^{*}}-\frac{\mu}{q}\nabla B\times\frac{\hat{\boldsymbol{b}}}{B_{||}^{*}},\tag{29}$$

where $B_{||}^{*}=\hat{\boldsymbol{b}}\cdot\boldsymbol{B}^{*}$. Now, using the identity

$$(\hat{\boldsymbol{b}}\times\boldsymbol{B}^{*})\times\hat{\boldsymbol{b}}=(\hat{\boldsymbol{b}}\cdot\hat{\boldsymbol{b}})\boldsymbol{B}^{*}-(\boldsymbol{B}^{*}\cdot\hat{\boldsymbol{b}})\hat{\boldsymbol{b}},$$

we can write

$$\boldsymbol{B}^{*}=\underbrace{(\boldsymbol{B}^{*}\cdot\hat{\boldsymbol{b}})}_{B_{||}^{*}}\hat{\boldsymbol{b}}+(\hat{\boldsymbol{b}}\times\boldsymbol{B}^{*})\times\hat{\boldsymbol{b}}.$$

In the second term $\boldsymbol{B}^*$, insert Eq. (27). This gives

$$\boldsymbol{B}^* = B_{||}^* \hat{\boldsymbol{b}} + \frac{m v_{||}}{q} \left[ \hat{\boldsymbol{b}} \times \left( \nabla \times \hat{\boldsymbol{b}} \right) \right] \times \hat{\boldsymbol{b}}.$$

Inserting the result from the following identity

$$\underbrace{\nabla(\hat{\boldsymbol{b}} \cdot \hat{\boldsymbol{b}})}_{=0} = 2(\hat{\boldsymbol{b}} \cdot \nabla)\hat{\boldsymbol{b}} + 2\hat{\boldsymbol{b}} \times (\nabla \times \hat{\boldsymbol{b}}) \implies \hat{\boldsymbol{b}} \times (\nabla \times \hat{\boldsymbol{b}}) = (\hat{\boldsymbol{b}} \cdot \nabla)\hat{\boldsymbol{b}},$$

gives

$$\boldsymbol{B}^* = B_{||}^* \hat{\boldsymbol{b}} - \frac{m v_{||}}{q} \underbrace{\hat{\boldsymbol{b}} \cdot \nabla}_{\nabla_{||}} \hat{\boldsymbol{b}} \times \hat{\boldsymbol{b}}.$$

Inserting this and $\mu = m v_\perp^2 / 2B$ into Eq. (29) we finally arrive at

$$\dot{\boldsymbol{X}} = v_{||} \hat{\boldsymbol{b}} + \frac{m \hat{\boldsymbol{b}}}{q B_{||}^*} \times \left( \frac{v_\perp^2}{2B} \nabla B + v_{||}^2 \nabla_{||} \hat{\boldsymbol{b}} \right). \tag{30}$$

In this equation for the guiding-center, the first term, $v_{||}\hat{\boldsymbol{b}}$, gives the motion along the field lines while the second term gives the guiding-center drifts and can be compared with the drift equations (13) and (15).

In a similar way the Eq. (28) can be solved in terms of $\dot{v_{||}}$ by doing a scalar multiplication with $\boldsymbol{B}^*$. This results in the expression

$$\dot{v_{||}} = -\frac{\mu \boldsymbol{B}^*}{m B_{||}^*} \cdot \nabla B. \tag{31}$$

The guiding-center equations of motion are thus given by Eq. (30) and (31).

# 3 Numerical methods

Since the purpose of this project is to simulate charged particle motion in a fusion plasma, knowledge about various numerical methods is necessary. In this section we will look at the theory and parts constituting the simulation program developed.

As mentioned earlier, equations of motion that include a complicated magnetic field have to be solved numerically. The magnetic field from ITER, to be used in the following simulations, certainly falls into this category. The magnetic field data used in this project was given in matrix form with values separated by double spaces, and had been calculated with a magnetic equilibrium solver that solves the Grad-Shafranov equations [11], which describe a magnetohydrodynamic equilibrium in a toroidally symmetric system. The magnetic field is accordingly toroidally symmetric. A second data file was also provided, containing information about the wall shape of the device, which is also toroidally symmetric. A brief introduction to the contents of the data is given in Section 3.1.

The numerical integration of the equations of motion is done by an ODE solver. The solver implemented here uses a Runge-Kutta method, which will be described in Section 3.2. In Section 3.3, we proceed to present the method used to determine whether the simulated particle collides with the device walls. Finally, in Section 3.4, an overview of the simulation tool developed as part of this project is given.

All plots were made using the programming language Python and the library `matplotlib` [12].

## 3.1 Magnetic field data

In order to make physically relevant simulations, magnetic field data from ITER was used in the simulation program. The data file contained three matrices, the field in cylindrical coordinates: $B_R(R,z), B_\phi(R,z)$ and $B_z(R,z)$. A contour plot of the projection of the magnetic field lines onto the $R-z$ plane, with the device wall superimposed over the field, is shown in Fig. 5a. The $R-z$ plane is the poloidal plane. Because of the toroidal symmetry of the device and the magnetic field, the azimuthal coordinate has been neglected in Fig. 5, as the most interesting information comes from looking at the field in the poloidal plane. Concentric, closed field lines fill up most of the device. At the edges, mostly the left side and the bottom, the field lines are open. Note especially the position of the magnetic field axis in 5a, which is approximately at $R = 6.7\,\mathrm{m}$, $z = 0.5\,\mathrm{m}$. The entire device wall, plotted in 3D, can be seen in Fig. 1. The wall data consisted of a number of $(R,z)$-points indicating the wall contour.

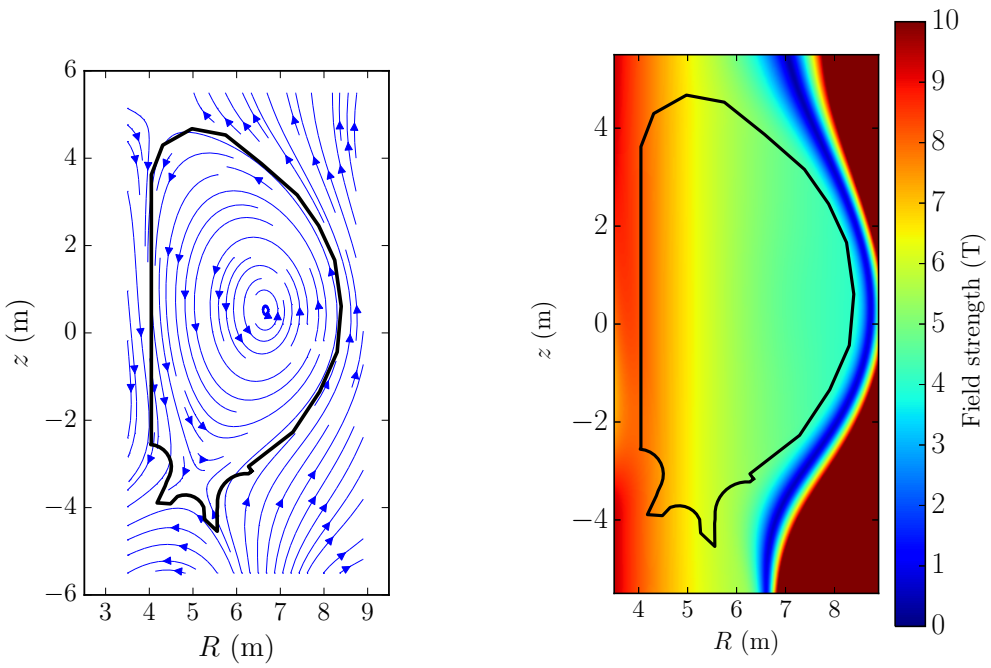


**(a)** Magnetic field lines **(b)** Magnetic field strength

**Figure 5:** Two different views of the ITER magnetic field. In (a), the magnetic field lines in the poloidal plane, with directional arrows, have been plotted, while in (b) the magnetic field strength $B = |\boldsymbol{B}|$ is shown, also in the poloidal plane. In both plots, the ITER wall contour has been superimposed to show the boundaries of the device. Note especially how the field strength decreases with $R$.

Another important quantity of the magnetic field is the magnetic field strength $B = |\boldsymbol{B}|$. The field strength plays an important role for the guiding-center equations of motion, and has been plotted in a color map in Fig. 5b.

When analyzing the system analytically, one can use the fact that the magnetic field of ITER behaves approximately like that for a toroid wound in current-carrying wire.[1] Using Ampere's law, we find an approximation for the magnetic field strength in a point with cylindrical coordinates $(R, z)$ to be (see for example Cheng (2014) [13])

$$B(R) \approx \frac{B_0 R_0}{R}, \tag{32}$$

where $B_0$ is the magnetic field strength at the arbitrary point $R_0$. This expression predicts that the field strength will be inversely proportional to the radial distance from the axis of symmetry, of the device, i.e. the middle of the toroid. By looking at Fig. 5b we can rather easily convince ourselves of the validity of this approximation, as the field seems to decrease monotonically with $R$.

## 3.2 Time integration method

The basic idea for any routine for solving an ordinary differential equation (ODE) with initial value boundary conditions (called an *initial value problem*, IVP) is to start at the initial values, and then take steps in the direction dictated by the func-

[1] In reality, there are additional features to the magnetic field, but these are generally small compared to the toroidal magnetic field and can, for our purposes, be neglected.

tion corresponding to the derivative. This is the function $\boldsymbol{f}$ in Eq. (33). For small steps, a good approximation to the underlying differential equation is achieved [14].

Consider an IVP over the time interval $[t^{(0)}, t^{(f)}]$,

$$\begin{cases} \dot{\boldsymbol{z}} = \boldsymbol{f}(t, \boldsymbol{z}), \\ \boldsymbol{z}\left(t^{(0)}\right) = \boldsymbol{z}^{(0)}. \end{cases} \tag{33}$$

To obtain a numerical approximation of the solution $\boldsymbol{z}$, the interval $[t^{(0)}, t^{(f)}]$ is divided into $N$ equal subintervals. Mesh points $t^{(j)} = t^{(0)} + jh,\ j = 1, \ldots, N$ are selected, where

$$h = \frac{t^{(f)} - t^{(0)}}{N},$$

is the step size. One of the simplest numerical procedures to solve an IVP is the *Euler forward* method, which is a first-order integration scheme. Its formula is

$$\boldsymbol{z}^{(n+1)} = \boldsymbol{z}^{(n)} + h\boldsymbol{f}(t^{(n)}, \boldsymbol{z}^{(n)}).$$

The Euler forward method is not recommended for practical use due to its poor accuracy compared to other methods with an equivalent step size, it is also not very stable. However, information from several Euler-type steps can be combined to obtain a higher order method. This is the basis for Runge-Kutta methods.

Runge-Kutta numerical methods are a family of one-step methods for solving first order ODEs, using function values in multiple stages within one step. The Euler forward method is equivalent to a first stage Runge-Kutta method. One of the most powerful and most used Runge-Kutta methods is the four-stage (RK4), which is of order four: $\mathcal{O}(h^4)$. This is often used in conjunction with an adaptive step size algorithm. A common variant is the Runge-Kutta-Fehlberg method (RKF45) that has an error estimate of order five, $\mathcal{O}(h^5)$. That is the one we will use. A more in-depth look at this method will now follow. For further information we refer the reader to *Numerical Recipes in C* [15].

An explicit Runge-Kutta (RK) method of the $m$th stage is given by

$$\boldsymbol{z}^{(n+1)} = \boldsymbol{z}^{(n)} + h\sum_{i=1}^{m} a_{mi}\boldsymbol{k}_i,$$

with

$$\begin{aligned} \boldsymbol{k}_1 &= \boldsymbol{f}\left(t^{(n)}, \boldsymbol{z}^{(n)}\right), \\ \boldsymbol{k}_2 &= \boldsymbol{f}\left(t^{(n)} + c_2 h, \boldsymbol{z}^{(n)} + h a_{21}\boldsymbol{k}_1\right), \\ &\vdots \\ \boldsymbol{k}_m &= \boldsymbol{f}\left(t^{(n)} + c_m h, \boldsymbol{z}^{(n)} + h\sum_{i=1}^{m-1} a_{mi}\boldsymbol{k}_i\right), \end{aligned}$$

for coefficients $a_{ij}$, $b_k$ and $c_j$. These are arranged in a so called Butcher tableau, as shown in Table 1. The specific coefficients used for this method are the Fehlberg parameters that can be seen in Table 2. The parameters are acquired by solving

**Table 1:** A generic Butcher Tableau.

| | | | | | |
|---|---|---|---|---|---|
| $0$ | | | | | |
| $c_2$ | $a_{21}$ | | | | |
| $c_3$ | $a_{31}$ | $a_{32}$ | | | |
| $\vdots$ | $\vdots$ | $\vdots$ | $\ddots$ | | |
| $c_m$ | $a_{s1}$ | $a_{m2}$ | $\cdots$ | $a_{m,m-1}$ | $a_{m,m}$ |
| | $b_1$ | $b_2$ | $\cdots$ | $b_{m-1}$ | $b_m$ |
| | $\hat{b}_1$ | $\hat{b}_2$ | $\cdots$ | $\hat{b}_{m-1}$ | $\hat{b}_m$ |

**Table 2:** Fehlberg parameters for the RKF45 method.

| | | | | | | |
|---|---|---|---|---|---|---|
| $1/4$ | $1/4$ | $0$ | $0$ | $0$ | $0$ | $0$ |
| $3/8$ | $3/32$ | $9/32$ | $0$ | $0$ | $0$ | $0$ |
| $12/13$ | $1932/2197$ | $-7000/2197$ | $7296/2197$ | $0$ | $0$ | $0$ |
| $1$ | $439/216$ | $-8$ | $3680/513$ | $-845/4104$ | $0$ | $0$ |
| $1/2$ | $-8/27$ | $2$ | $-3544/2565$ | $1859/4104$ | $-11/40$ | $0$ |
| | $25/216$ | $0$ | $1408/2565$ | $2197/4104$ | $-1/5$ | $0$ |
| | $16/135$ | $0$ | $6656/12825$ | $28561/56430$ | $-9/50$ | $2/55$ |

a system of algebraic equations that comes from comparing coefficients of Taylor series expansions of $\dot{\boldsymbol{z}} = \boldsymbol{f}(t, \boldsymbol{z})$ and the $\boldsymbol{k}$-vectors.

Accuracy is improved with decreasing step size $h$, but this comes with the drawback of longer computation time. To optimize the step size, an adaptive step size control algorithm is implemented. At each step, two different approximations of the solution are made and compared, one of order four (denoted as $\boldsymbol{z}^{(n+1)}$) and one of order five (denoted as $\hat{\boldsymbol{z}}^{(n+1)}$). The estimated error for each vector component

$$\varepsilon_j = \left| z_j^{(n+1)} - \hat{z}_j^{(n+1)} \right|,$$

is compared to a desired accuracy $\varepsilon_0$. If any $\varepsilon_j > \varepsilon_0$, the step size is decreased, and if any $\varepsilon_j < \varepsilon_0$, the step size is increased. The reason for calculating separate errors for each component is that their values can differ in orders of magnitude, as in our application. So it is necessary to have separate measures for the error to ensure that the adaptive step size algorithm functions properly.

Here a fourth-order Runge-Kutta method with five stages is used along with a fifth-order method with six stages. For six stages there are six $\boldsymbol{k}$-vectors:

$$\begin{aligned}
\boldsymbol{k}_1 &= \boldsymbol{f}\left(t^{(n)}, \boldsymbol{z}^{(n)}\right), \\
\boldsymbol{k}_2 &= \boldsymbol{f}\left(t^{(n)} + c_2 h, \boldsymbol{z}^{(n)} + h a_{21} \boldsymbol{k}_1\right), \\
&\vdots \\
\boldsymbol{k}_6 &= \boldsymbol{f}\left(t^{(n)} + c_6 h, \boldsymbol{z}^{(n)} + h \sum_{j=1}^{5} a_{6j} \boldsymbol{k}_j\right).
\end{aligned}$$

The embedded fourth-order formula is

$$\boldsymbol{z}^{(n+1)} = \boldsymbol{z}^{(n)} + h\sum_{i=1}^{5} b_i \boldsymbol{k}_i,$$

and a better value is determined using the fifth-order method

$$\hat{\boldsymbol{z}}^{(n+1)} = \hat{\boldsymbol{z}}^{(n)} + h\sum_{i=1}^{6} \hat{b}_i \boldsymbol{k}_i.$$

Using the coefficients from the Butcher tableau, the error estimate for each component $\varepsilon_j$ can be calculated as

$$\varepsilon_j = \left| z_j^{(n+1)} - \hat{z}_j^{(n+1)} \right| = \left| \sum_{i=1}^{6} (b_i - \hat{b}_i)(\boldsymbol{k}_i)_j \right|.$$

The optimal step size change is given by

$$h_{\text{opt}} = \begin{cases} \beta h \left(\frac{\varepsilon_0}{\varepsilon}\right)^{1/5}, & \varepsilon_j \geq \varepsilon_0 \\ \beta h \left(\frac{\varepsilon_0}{\varepsilon}\right)^{1/4}, & \varepsilon_j < \varepsilon_0 \end{cases} \tag{34}$$

where $\beta \simeq 1$ is a "safety factor", because our error estimate is not exact. Usually $\beta = 0.8$ or $\beta = 0.9$. This is used to further ensure that a small enough step is taken.

The correctness of our implementation of this solver was tested by solving the Lotka-Volterra equations [16], also known as the predator-prey equations. The solution to these equations is well known.

## 3.3 Domain check

In order to produce realistic simulations of particle trajectories, it is important to remember that there exists a constraint on the particle position; the particle has to be inside the device at all times. Thus an algorithm to check whether the particle has collided with the device wall, needs to be constructed. One of the simplest ways to do this is by checking whether certain line segments intersect [17].

Assume that the path the particle takes to travel from one point $u_0 = (x_0, y_0)$ to $u_1 = (x_1, y_1)$ can be represented by a parametrization

$$u(t) = u_0 + t(u_1 - u_0)\ , \qquad t \in [0, 1].$$

Now, suppose that the wall contour is represented by the coordinates $(\tilde{x}_i, \tilde{y}_i)_{i=0}^{N}$, where $N$ is the total number of points. Assume that a parametrization can be done of the line connecting the point $n_i$: $v_0 = (\tilde{x}_i, \tilde{y}_i)$ and the closest neighbor (in a certain direction) $v_1 = (\tilde{x}_{i+1}, \tilde{y}_{i+1})$. The parametrization for this line is then of the form

$$v(s) = v_0 + s(v_1 - v_0)\ , \qquad s \in [0, 1].$$

If the particle path is intersecting this part of the contour, there exist a point $p \in \Omega$ such that $u(t) = p = v(s)$ equivalent to $u_0 + t(u_1 - u_0) = v_0 + s(v_1 - v_0)$. Here $\Omega$ is the domain of the device. By using each coordinate representation in $x$'s and $y$'s, the equation can be rewritten in matrix form as

$$\underbrace{\begin{pmatrix} x_1 - x_0 & \tilde{x}_i - \tilde{x}_{i+1} \\ y_1 - y_0 & \tilde{y}_i - \tilde{y}_{i+1} \end{pmatrix}}_{A} \underbrace{\begin{pmatrix} t \\ s \end{pmatrix}}_{\boldsymbol{x}} = \underbrace{\begin{pmatrix} x_0 - \tilde{x}_i \\ y_0 - \tilde{y}_i \end{pmatrix}}_{\boldsymbol{b}}. \tag{35}$$

This matrix-equation has a unique solution if the determinant of $A$ is nonzero. Thus

$$\det(A) = \begin{vmatrix} x_1 - x_0 & \tilde{x}_i - \tilde{x}_{i+1} \\ y_1 - y_0 & \tilde{y}_i - \tilde{y}_{i+1} \end{vmatrix} = (x_1 - x_0)(\tilde{y}_i - \tilde{y}_{i+1}) - (\tilde{x}_i - \tilde{x}_{i+1})(y_1 - y_0) \neq 0.$$

The solution is then given by $\boldsymbol{x} = A^{-1}\boldsymbol{b}$ where $A^{-1}$ is

$$A^{-1} = \frac{1}{\det(A)} \begin{pmatrix} \tilde{y}_i - \tilde{y}_{i+1} & \tilde{x}_{i+1} - \tilde{x}_i \\ y_0 - y_1 & x_1 - x_0 \end{pmatrix}.$$

By doing the matrix multiplication the resulting equations become

$$\begin{pmatrix} t \\ s \end{pmatrix} = \frac{1}{\det(A)} \begin{pmatrix} \tilde{y}_i - \tilde{y}_{i+1} & \tilde{x}_{i+1} - \tilde{x}_i \\ y_0 - y_1 & x_1 - x_0 \end{pmatrix} \begin{pmatrix} x_1 - x_0 & \tilde{x}_i - \tilde{x}_{i+1} \\ y_1 - y_0 & \tilde{y}_i - \tilde{y}_{i+1} \end{pmatrix} =$$
$$= \frac{1}{\det(A)} \begin{pmatrix} (\tilde{y}_i - \tilde{y}_{i+1})(x_1 - x_0) + (\tilde{x}_{i+1} - \tilde{x}_i)(y_1 - y_0) \\ (y_0 - y_1)(\tilde{x}_i - \tilde{x}_{i+1}) + (x_1 - x_0)(\tilde{y}_i - \tilde{y}_{i+1}) \end{pmatrix}.$$

Whenever there exists a solution to (35) such that

$$\begin{cases} t = & (\tilde{y}_i - \tilde{y}_{i+1})(x_1 - x_0) + (\tilde{x}_{i+1} - \tilde{x}_i)(y_1 - y_0) \\ s = & (y_0 - y_1)(\tilde{x}_i - \tilde{x}_{i+1}) + (x_1 - x_0)(\tilde{y}_i - \tilde{y}_{i+1}) \end{cases} \qquad t, s \in [0, 1],$$

for $0 \leq i \leq N$, then the particle path intersects the device contour, which indicates that the particle has collided with the device.

## 3.4 Program workflow

In the previous two subsections, the algorithms we have written were presented. Here, the workflow of the complete program will be described and illustrated by a flow chart. First, two things need to be mentioned.

To be able to get magnetic field data for every single point in the device the discrete data has to be interpolated. A two-dimensional interpolation library called `Interp2d` [18] was used for this purpose. This library also contains functions for differentiation, which were used to calculate derivatives of the magnetic field for the guiding-center method.

Second, the equations of motion were derived for a Cartesian coordinate system. This was done to avoid the more complicated expressions for derivatives of fields in curvilinear coordinates. However, by virtue of the toroidal symmetry of the tokamak, cylindrical coordinates are preferred. The magnetic field data was given in cylindrical coordinates, so coordinate transformations had to be done. This step is not shown explicitly in the flow chart.

The program works as follows:

- Read input data containing the simulation time $t_{\text{end}}$, particle mass, charge, initial position and velocity. The magnetic and domain data files are also given as inputs, as well as a flag indicating whether you want to solve for particle or guiding-center motion.
- Read and store this data, passing the field data to the interpolator.
- Check if the initial position is inside the device. If no, stop.
- If yes, choose which problem to solve and store the respective initial values.
- Start the time integrator, run until it reaches $t_{\text{end}}$.
- Check if memory is allocated for solution data, if not, allocate.
- Take one step with the integrator by calculating all variables for the time $t+h$, where $h$ is the time step length.
- Check if the error is small enough. If not, calculate the next position and velocity for a smaller time step.
- If yes, check if the new position is inside the allowed domain.
- If yes, repeat until $t_{\text{end}}$ is reached. Then write the solution data to file.
- If no, exit with a message saying the particle has hit the wall and write the solution data acquired so far to file.

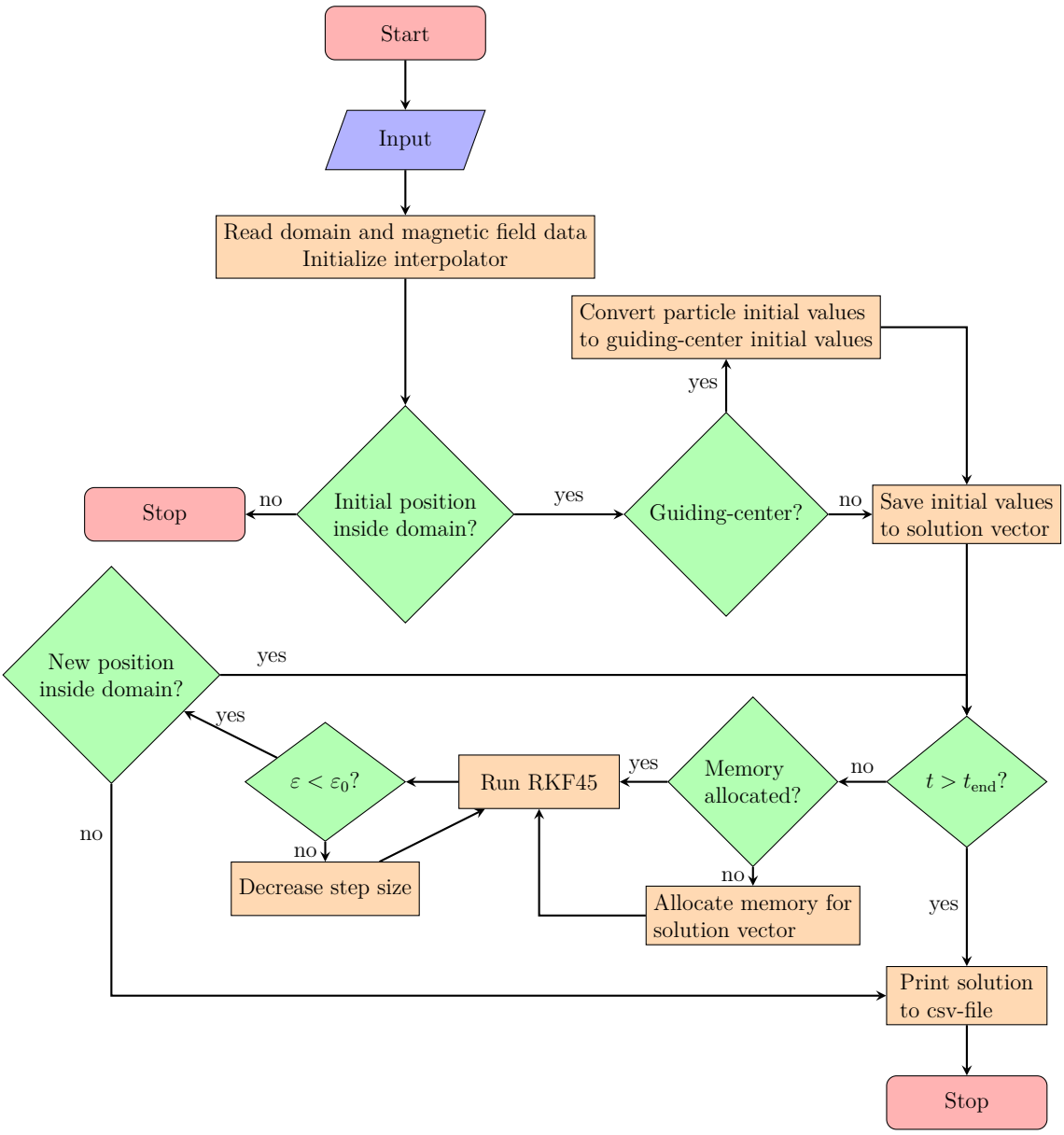


All of our code can be found at `https://github.com/eerosdisciples`. The QR-code leads to this website. For more thorough instructions on how to run the program, please consult Appendix D.

# 4 Simulation of particle orbits

As part of this project, a computer program for calculating particle orbits was developed, using the theory presented in the previous sections. In this section we will now use that tool to study the orbits of different charged particles that may be found in fusion plasmas. The purpose of this section is to understand how the properties of different particles affect their motion within the tokamak, and also to explain the reasons for the peculiarities of their orbits.

In order to make physically relevant simulations, we will need to know certain properties of fusion plasmas. The simulation tool used requires particle parameters such as mass, charge and initial velocity to be given. For this reason we should find the typical values of these parameters in fusion plasmas. Since, by definition, a plasma is ionized, it will contain free electrons (mass $m \approx 5.49 \cdot 10^{-4}\,\mathrm{u}$, charge $q = -e$) and ions. In ITER, a plasma consisting of the two hydrogen isotopes deuterium ($^2$H or $D^+$) and tritium ($^3$H or $T^+$) will be used, leading us to believe that a large portion of the ions within the plasma will have mass $m \approx 2$ - $3\,\mathrm{u}$ and charge $q = e$. In a typical fusion plasma of temperature $1 - 10\,\mathrm{keV}$ [19], these particles will have energies in the region $1 - 10\,\mathrm{keV}$. However, it turns out that the characteristics of the particle orbits for $D^+$ and $T^+$ become visible (compared to the scale of the device) first at higher energies, and so most particles in this section will be given energies in the MeV scale. The use of these high energies are not entirely unphysical though, as such high energy ions can actually originate from neutral beams used for plasma heating.

Other common particles within fusion plasmas are the helium ions called alpha particles (mass $m \approx 4\,\mathrm{u}$, charge $q = 2e$), which are produced in the nuclear reactions. They are generated at the energy of $3.5\,\mathrm{MeV}$. Because they are fusion products they will have much more kinetic energy than the average plasma temperature.

Apart from the particles just described, certain impurities will also be present. In particular, we can expect to find carbon ions, $C^{6+}$ (mass $m \approx 12\,\mathrm{u}$, charge $q = 6e$), and tungsten ions, $W^{56+}$ (mass $m \approx 184\,\mathrm{u}$, charge $q = 56e$), which originate from the components facing the plasma and from the wall of the reactor. Since these particles do not originate from nuclear reactions, they will have energies in the same order as the plasma temperature, $1 - 10\,\mathrm{keV}$.

Except for the electron, all particles described so far have positive charges. In order to illustrate an interesting property of the orbit, we will however need a particle with a negative charge. The electron could in principle be used, but due to its small mass the effect would require us to look very closely at the particle orbit in order to see it. Because of this, we also introduce a particle called *protide*. This particle is a hydrogen isotope, consisting of one proton and two electrons, thus having mass $m \approx 1\,\mathrm{u}$ and charge $q = -e$. In a real fusion plasma, this particle will be extremely rare and short-lived, if at all present. The use of the particle in this project is rather motivated by its mass and charge, which happens to give interesting results.

## 4.1 Observed orbit topologies

Knowing what particles we may expect to find in a plasma, and that the magnetic field will lock them to an orbit, a natural question would be what these orbits will look like. From the theory derived in Section 2, we would expect the orbits to look a bit different for different particles, depending on their mass, charge, initial position

and initial velocity. Using the simulation tool developed in this project, we have been able to simulate both the particle and guiding-center orbits for different particles, and in the present section our findings from these simulations will be presented. A deeper analysis of these observations will be postponed until Section 4.2.

A simple test of the program in which we place an alpha particle at $R = 8.0287\,\mathrm{m}$ and $z = 0.2538\,\mathrm{m}$, and give it a kinetic energy of $E = 3.5\,\mathrm{MeV}$, yields the orbits shown in Fig. 6, depending on how its initial velocity vector is directed. The simulation program calculates either the particle's coordinates (the black orbits in Fig. 6) or the corresponding guiding-center coordinates (the red orbits in Fig. 6) in three dimensions (hence the three-dimensional plots in the upper part of the figure), but as can be seen from the lower parts of the figure, the orbits may advantageously be plotted in the two-dimensional $R$-$z$ (poloidal) plane, which turns out to be much easier to work in. The reason for this is simply that the magnetic field used is symmetric in the azimuthal angular coordinate (assuming cylindrical or similar coordinates are used), and so our three-dimensional geometry can be reduced to a simpler two-dimensional one. It can be worth noting that on top of the banana motion, the orbits have a precession around the tokamak. This information is lost in the 2D figure. This may be important, because as the trapped electrons do their precession around the tokamak, they can get in resonance with drift waves and can generate instabilities (so called trapped electron modes). Nonetheless, this is not encompassed by this project and we proceed to the analysis of only 2D figures.

Fig. 6 shows the two most common orbits found in tokamaks, labeled *banana* and *passing* orbits (Fig. 6a/6c and 6b/6d, respectively). Particles following a banana orbit are commonly referred to as *trapped* particles, while particles following a passing orbit are simply referred to as *passing*, or *circulating*, particles. These are the only two orbit topologies we will encounter, and we will see that they are closely linked. As mentioned above, the only difference between the orbits is how the particle's initial velocity is directed. A measure of this is the quantity $\xi$, that can be defined as

$$\xi = v_\parallel / v, \tag{36}$$

which will become a powerful tool in the analysis of the transitions between banana and passing orbits. We will only be interested in the value of $\xi$ at the beginning of the orbit, and so will denote it by $\xi_0$ in order to distinguish it from the continuously changing $\xi$.

As can be seen in Fig. 6 (with some effort), the particle orbits form bent helices that follow the corresponding guiding-center orbits. A magnification of the particle's orbit is also shown in Fig. 7, where the helix shape is more prominent. The magnification reveals an interesting feature of the particle's orbit, which we shall return to later, namely the fact that the guiding-center seems to slow down at the "banana tips" (called *mirror points*), i.e. the particle's velocity parallel to the magnetic field lines decreases.

### 4.1.1 Orbit width

The two simplest parameters that can be varied in the program are the mass and charge of the particle to be simulated. This section will be dedicated to the study of how these two parameters affect the particle's orbit. In order to have physically relevant results, as far as possible, some the most common kinds of particles found

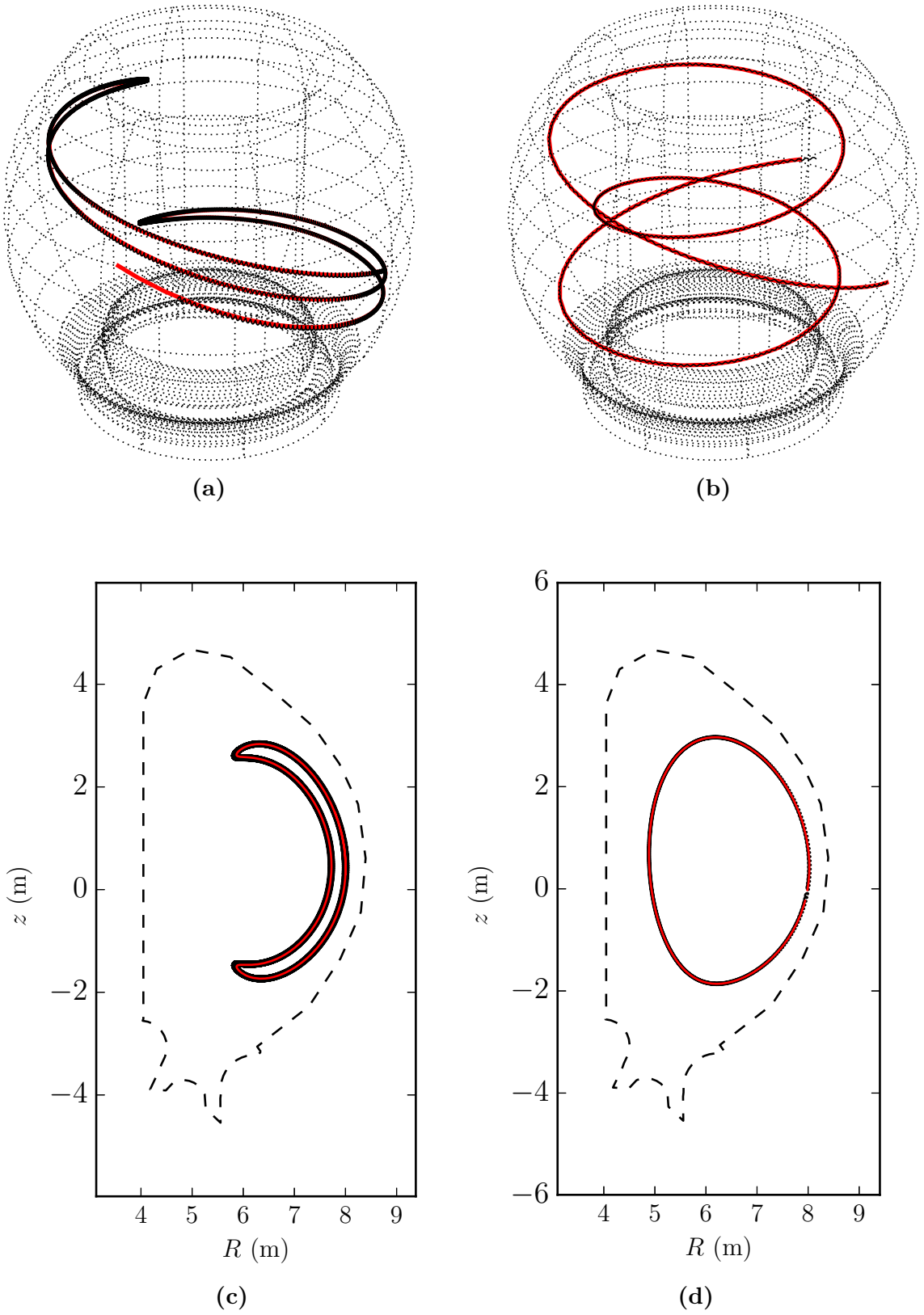


**Figure 6:** Example orbits for an alpha particle with energy 3.5 MeV. All four plots show the orbit that the particle follows (black), as well as the orbit that the guiding-center follows (red), both of which are calculated using the tool developed as part of this project. The orbits presented in these figures are classified as either banana orbits ((a) and (c)), or passing orbits ((b) and (d)). As can be seen, 2D plots are usually easier to work with, and also give a hint about where the orbits get their names from.

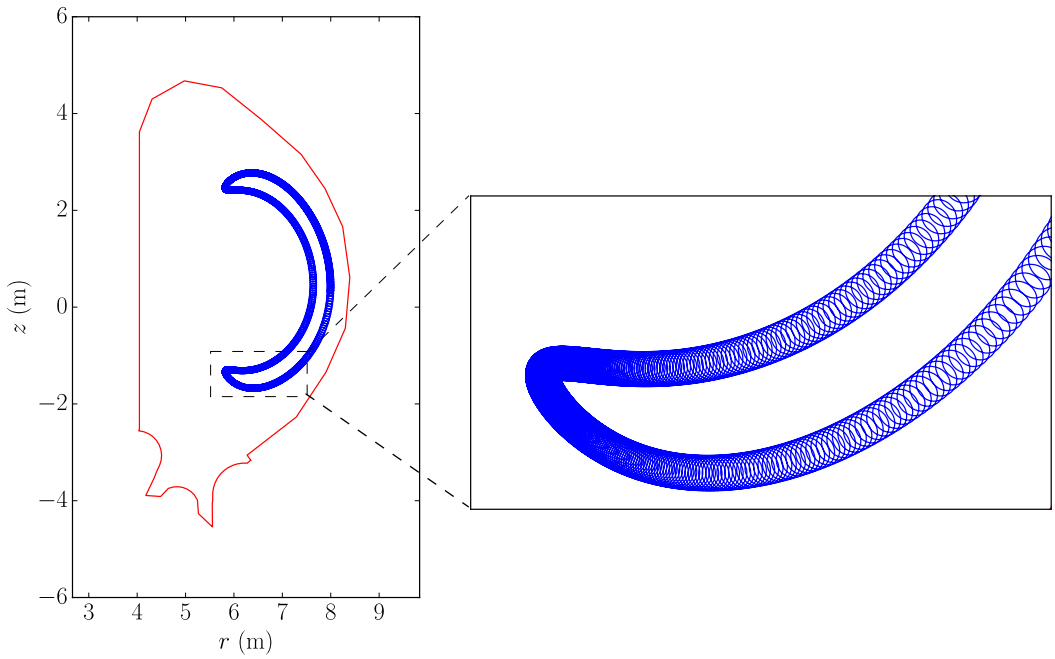


**Figure 7:** Magnification of the banana orbit for an alpha particle with kinetic energy 3.5 MeV. Here, the helix shape of the particle's orbit becomes apparent, motivating the guiding-center transformation. As can be seen, the velocity parallel to the magnetic field appears to decrease as the particle approaches the mirror points of the banana.

in fusion plasmas will be used in simulations. These are alpha particles, deuterium ($D^+$), tritium ($T^+$), carbon ($C^{6+}$) and tungsten ($W^{56+}$). Note that since these are part of the plasma, they are all ionized and thus possess positive charges.

In Fig. 8, four different particles ($D^+$, $T^+$, $C^{6+}$, $W^{56+}$) have been simulated using the guiding-center method for the same energies $E = 1\,\text{MeV}$, initial position ($R = 8\,\text{m}$, $z = 0\,\text{m}$) and same $\xi_0 = 0.5$. The result is the four banana orbits shown, which all have different widths. From this figure we can immediately draw one important conclusion, namely that the banana width increases with an increased mass. This can be seen by comparing the orbits for $D^+$ (mass $m \approx 2\,\text{u}$) and $T^+$ (mass $m \approx 3\,\text{u}$), of which the $T^+$ orbit is somewhat wider. Knowing this, we can then also conclude that the width decreases for an increase in charge magnitude, which is easily seen by looking at the orbit for $W^{56+}$. The banana width must in other words be proportional to some ratio between mass and charge. A simple calculation reveals that this ratio cannot simply be $m/q$, and so we should instead expect it to be of the form $m^\alpha/q^\beta$, for $\alpha, \beta > 0$. This will be analyzed in more detail later in Section 4.2.

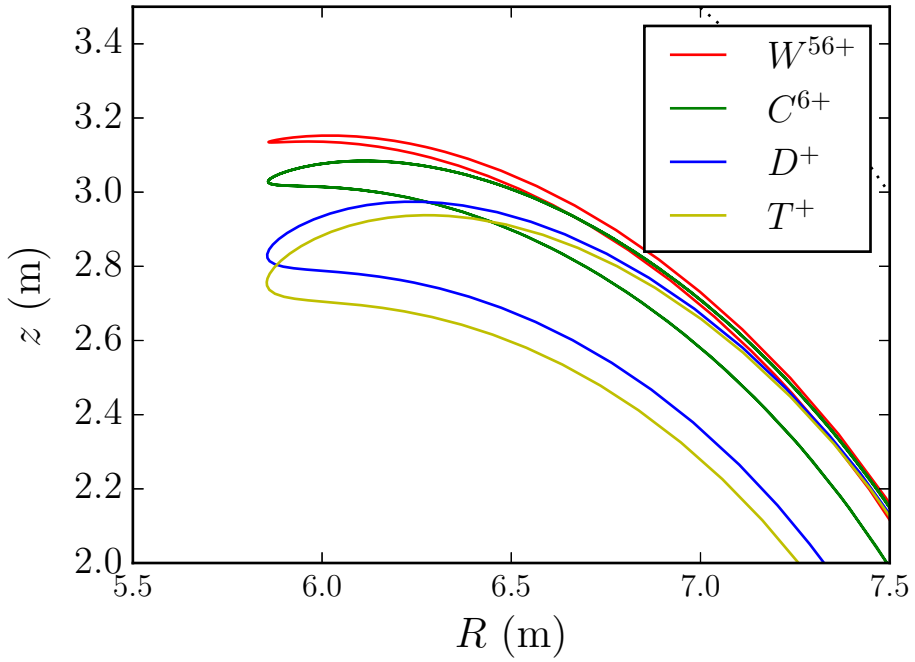


**Figure 8:** Four different guiding-center orbits for particles with energy 1 MeV, but with different mass/charge ratios. As can be seen, increased mass appears to result in a wider banana orbit, while increased charge appears to result in the opposite.

Fig. 8 shows several interesting properties of banana orbits, but one thing that cannot be seen is the effect of the charge sign. In order to study this we must turn to the somewhat unrealistic choice of the *protide* particle, consisting of one proton and two electrons, thus having mass $m \approx 1\,\mathrm{u}$ and charge $q = -e$.[2] Passing this particle, and a regular proton, to the guiding-center simulation program, giving them the same energies $E_- = E_+ = 1\,\mathrm{MeV}$ and initial positions, yields the orbits shown in Fig. 9 for $\xi_0 = 0.5$ and $\xi_0 = 0.7$, respectively. Arrows have been introduced in the plots to show in which directions the particles' guiding-centers follow the orbits.

As can be seen in Fig. 9a, depending on the sign of the particle's charge, the guiding-center banana orbit will turn either inwards (positive charge) or outwards (negative charge) at the mirror points. For the passing orbits in Fig. 9b we instead see how the sign of the charge causes the orbit to extend further towards the center of the fusion device. This gives a hint for what causes the banana to have a width, as it seems something is pushing the particle in different directions. We will see later that this is due to particle drifts, as discussed in Section 2.1.2. On a side note, if the sign of the initial value of the velocity is changed, you find orbits similar to when the sign of the particle charge is changed.

[2]The reason we are not simply using an electron is that its small mass causes the width of its banana orbit to make the effects we want to study virtually invisible, unless we zoom in very closely. Zooming in would however instead cause us to miss the effect of the protons charge sign

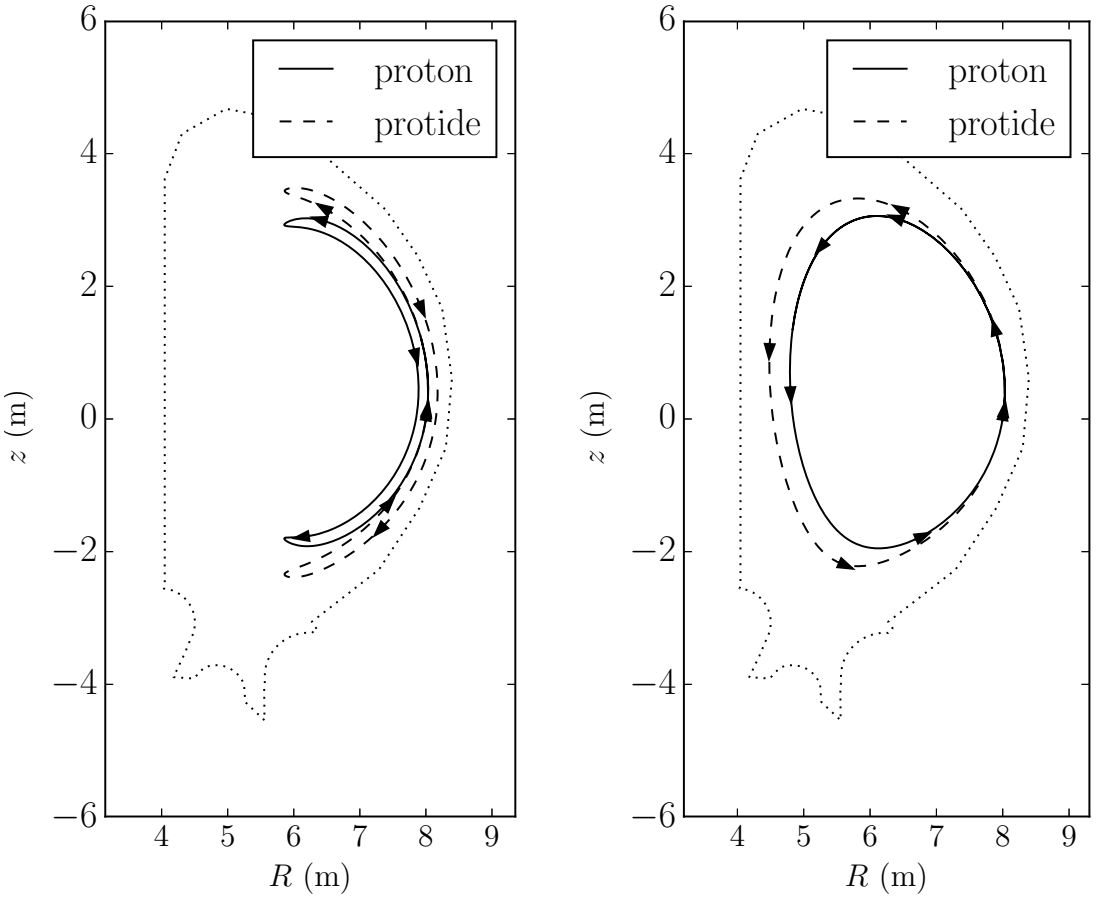


**(a)** Banana orbits

**(b)** Passing orbits

**Figure 9:** Examples of banana and passing orbits of an alpha particle and a protide, plotted in the same figures for reference. In both figures the particles' initial positions were $(R, z) = (8.0287, 0.2538)\,\mathrm{m}$ and their energies were $E = 3.5\,\mathrm{MeV}$. Note how the banana width of the protide is much thinner than that of the alpha particle. Also note that directions are opposite in the banana orbit, due to the difference of the particle charges.

### Importance of energy for banana width

So far we have simulated several different particles with the same energies. It turns out however, that also the energy of the particle affects the banana orbit width. In Fig. 10, three different alpha particles (mass $m \approx 4\,\mathrm{u}$, charge $q = 2e$) were simulated with energies $E_1 = 3.5\,\mathrm{MeV}$, $E_2 = 1\,\mathrm{MeV}$ and $E_3 = 350\,\mathrm{keV}$. The results strongly remind of those in Fig. 9, and so it seems that whatever causes the banana width is not just affected by the particle's mass and charge, but also by it's speed (since $E = mv^2/2$). We see in Fig. 10 how the banana width increases by an increase in energy, and so it would be reasonable to think that the banana width is proportional to some positive power of the energy. This will later be shown to be true in Section 4.2.

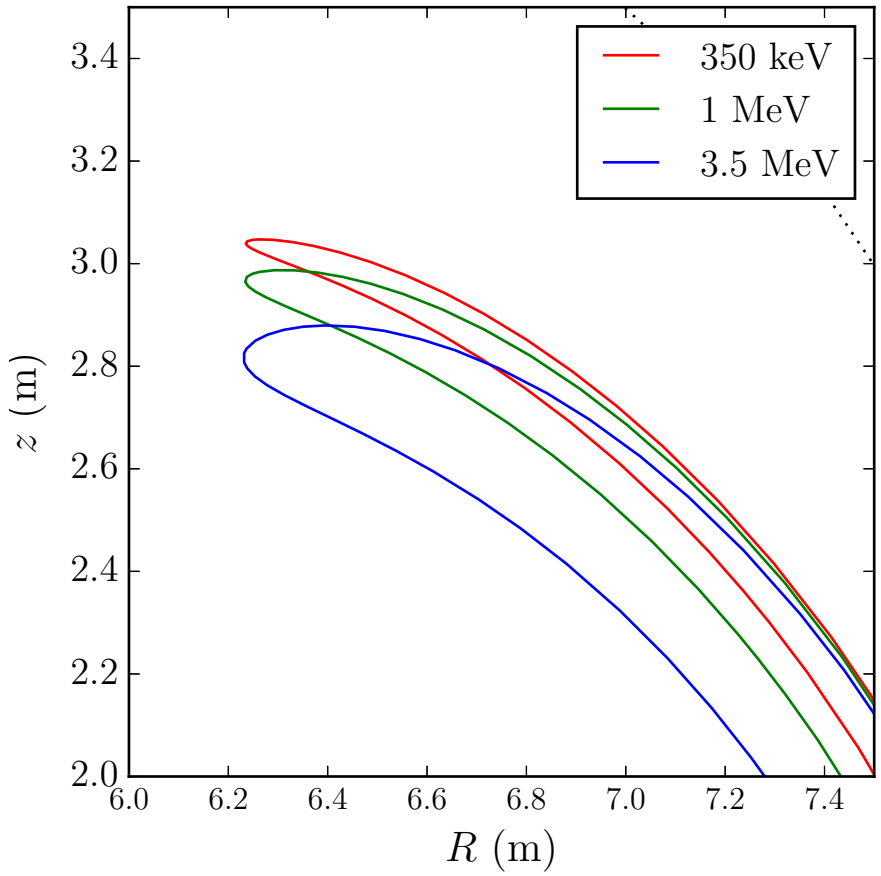


**Figure 10:** The guiding-center orbits for three different alpha particles with kinetic energies 3.5 MeV (red), 1 MeV (green) and 350 keV (blue). The value of $\xi_0$ was $\xi_0 = 0.5$. As can be seen, the banana width decreases as the particle's kinetic energy is decreased.

### 4.1.2 Deviation from field lines for banana orbits

Earlier in Section 2.1.2 we derived the different drifts that exist in a magnetized plasma. In this section we will continue with the observation of particle orbits, by studying how the different drifts affect the motion in terms of deviation from field lines, for a banana orbit.

With known coordinates of a certain field line, we define the deviation as the perpendicular distance from this field line to the trajectory of the particle. The coordinates of a certain field line can be obtained by removing all but the parallel motion in the direction of the magnetic field, however the particle is still experiencing the same mirror force, and will hence have a reflection for the same azimuthal angle.

In the simulations, all particles had energies of 10 keV as expected in a thermal plasma, apart from the alpha particle which had an energy of 3.5 MeV. The deviation was studied for one initial position of about $(R, z) = (6.8, 0)$ m and a value of $\xi_0 = -0.18$. The result can be found in Figures 11 and 12. Due to the large number of points that needed to be calculated, only the guiding-center method was used in Fig. 12. Note that since each particle will have a different velocity, a plot of the deviation as a function of time would result in displaced curves. Therefore, to assist the comparison, we parametrize the particle paths along the field line by the

index $i$. This way, we can more easily compare the deviations of the orbits from the magnetic field line.

At a first look we notice the rather unexpected local minimum which occurs between the points of maximum deviation for each particle. We also see that the minimum becomes less clear and finally disappears for lower values of the maximum deviation. When the particles have been reflected at the mirror point, they move backwards, but now on a different field line. Thus the result we see in Fig. 11 and 12 show that the field lines are not circularly symmetric around the center of the device. The longer the jump to a different field line, the greater the change of the field line curvature.

The next thing we recognize is that the deviation, and hence the drifts, are very different for particles with different mass, charge and energy. For the $T^+$ and $D^+$ particles, we have the same charge, but a difference in mass of about one atomic mass unit. For these, we see a slight change in the distance from the field line, where the maximum deviation is 18 % lower for the deuterium particle compared with tritium. We can conclude that when the mass is increased, so is the deviation from the field line.

However for the tungsten particle, having the highest mass, the deviation is quite low. The reason for this must be a higher value of charge, and thus a higher value of charge decreases the deviation.

Next, if we study the mass-to-charge ratio, we notice that while this value is the same for deuterium, carbon and alpha particles, the particle trajectories differ substantially. When looking at a fixed value of energy, we see that both the charge and the mass are increased by a factor of six for the carbon particle when compared to deuterium, while the value of the maximum deviation decreases by about 57 %. This means that the deviation value cannot be proportional to $m/q$, but either charge or mass, or both, must be raised to some power, as concluded in Section 4.1.1. The same observations hold for the tungsten particle, where the maximum deviation has decreased by about 85.3 %, when compared to tritium, while the mass-to-charge ratio has increased by about 10 %.

As a third observation, in Figures 11 and 12 we notice how the energy affects the deviation from the field lines. For the alpha particle with an energy of 3.5 MeV in Fig. 11, the deviation is ten times greater than for the other particles with lower energy in Fig. 12. Note the different scales in the figures. This suggests that the particle's deviation from the field lines increases with the energy.

In Fig. 11, both the guiding-center and the particle motion method has been used to simulate the alpha particle. Here we see that guiding-center seems to follow the center of the particle gyration almost perfectly, and the small differences that occur are probably due to error from the numerical calculations of the deviation from the field lines. This topic, comparing the guiding-center method and the particle motion, will be studied in detail in Section 4.3.

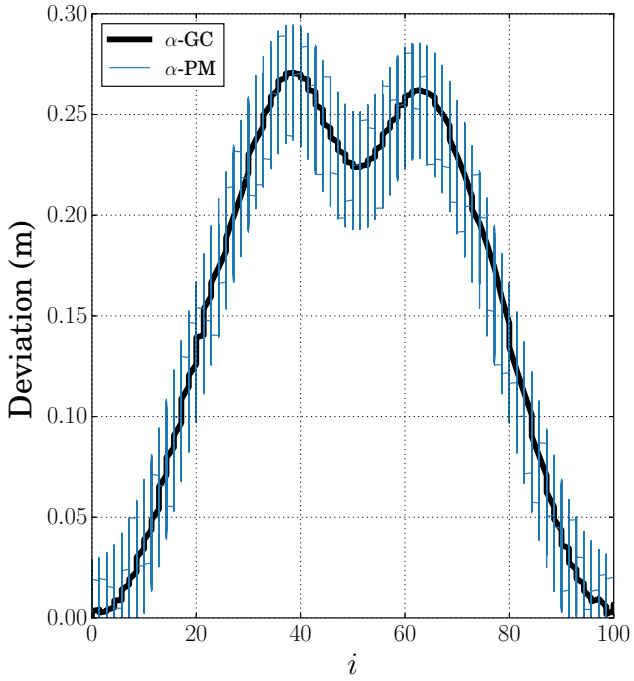


**Figure 11:** The deviation from the field lines for the alpha particle, during one banana orbit, simulated with both methods. The energy used for the simulations was 3.5 MeV. The index $i$ is used to parametrize the particle paths along the field line.

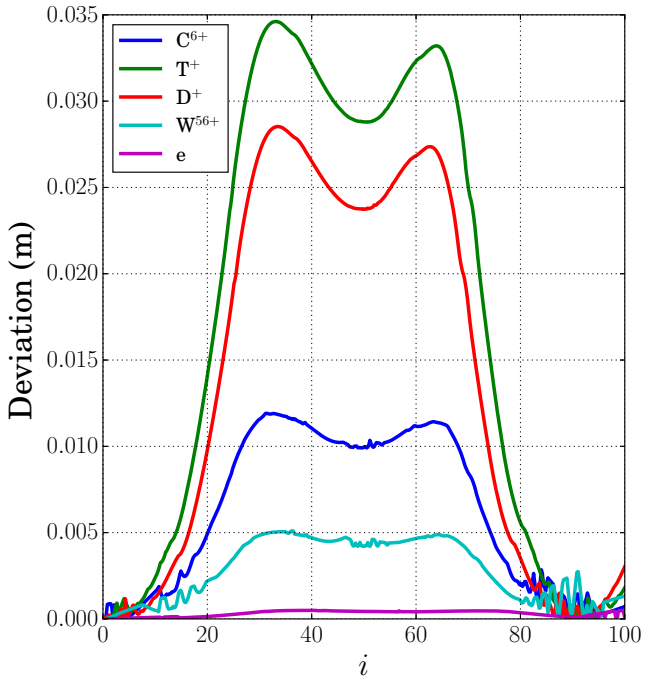


**Figure 12:** The deviation from the field lines for $D^+$, $T^+$, $C^{6+}$, $W^{56+}$ and $e^-$ particles during one banana orbit. The energies used for the simulations was 10 keV. The index $i$ is used to parametrize the particle paths along the field line.

### 4.1.3 Banana mirror points

Despite varying mass, charge and energy for particles, the banana mirror points remained constant in all figures above. This is also clearly seen in Figures 8 and 10. It follows that the type of orbit (banana or passing) is not affected by any of these parameters, but rather by some other parameter. It was mentioned briefly in the introduction to Section 4.1 that it is actually the direction of the particle's initial velocity that determines whether it will follow a banana or passing orbit. It was also mentioned that the quantity $\xi_0 = v_\parallel/v$ can be used as a measure for how the particle's initial velocity is directed. We will now study how variations of this parameter affects both the particle and its guiding-center orbits.

In Fig. 13, alpha particles with three different values of $\xi_0$ have been simulated at constant energy $E = 3.5\,\mathrm{MeV}$. The left part of the figure shows particle orbits, while the right part shows guiding-center orbits. The particle orbits in Fig. 13a seem to agree fairly well with the guiding-center orbits in Fig. 13b, possibly with the exception of the orbits for $\xi_0 = 0.6$. Here, the particle's orbit comes closer to the point we call the orbit's *transition point*, i.e. the point separating banana orbits from passing orbits. A suggested reason of why this deviation occurs is that the guiding-center approximation might have a small error compared with the exact particle motion. We remind that first order guiding-center theory is used here, for better accuracy higher order theory could be used. For larger values of $\xi_0$ this error seems to increase, which affects the mirror point coordinates and results in the observed deviation. This will be discussed in detail later in Section 4.3.

As can be seen in Fig. 13, a banana orbit will be successively stretched for increasing values of $\xi_0$, until its tips touch and the banana orbit turns into a passing orbit. It seems that the banana mirror point depends on $\xi_0$, and to understand why, we should look at how the particle/guiding-center energy behaves. First, let us split the total energy $E$ into two terms, $E = E_\parallel + E_\perp$, where $E_\parallel = mv_\parallel^2/2$ is the "parallel energy" and $E_\perp = mv_\perp^2/2 = \mu B$ the "perpendicular energy". These two terms tell us how much energy is stored in the motion along the magnetic field lines and perpendicular to the magnetic field lines, respectively. We already know from energy conservation that the particle's total energy must remain constant through the entire orbit, thus we would not get much interesting information from just looking at $E$. When we split the energy into parallel and perpendicular terms however, as has been done in Fig. 14a and Fig. 14b, we observe how these two terms actually vary over the course of the orbit and constantly balance each other.

There are several points of interest in Fig. 14, but possibly the most significant one is the fact that the parallel energy terms for the banana orbits drop to zero in the mirror points. Since $E = E_\parallel + E_\perp$, the perpendicular energy term $E_\perp$ must balance out the parallel term there, and thus accumulates all of the 3.5 MeV energy in the mirror points. We can also conclude from this information that, since the particle mass $m$ is constant, the parallel velocity $v_\parallel$ must also drop to zero at the mirror points. Likewise, the particle's perpendicular speed $v_\perp$ must increase to its maximum at the mirror points. By looking at the orbits, and keeping in mind that the orbit is approximately locked to the magnetic field lines, this allows us to conclude that the particle (or rather its guiding-center) must turn back in the direction it came. In other words, the parallel speed $v_\parallel = \boldsymbol{v} \cdot \hat{\boldsymbol{b}}$ must change sign.

For the orbits resulting from $\xi_0 = 0.7$ on the other hand, the parallel energy term never goes to zero. We see in Fig. 14 how, for both the particle and guiding-

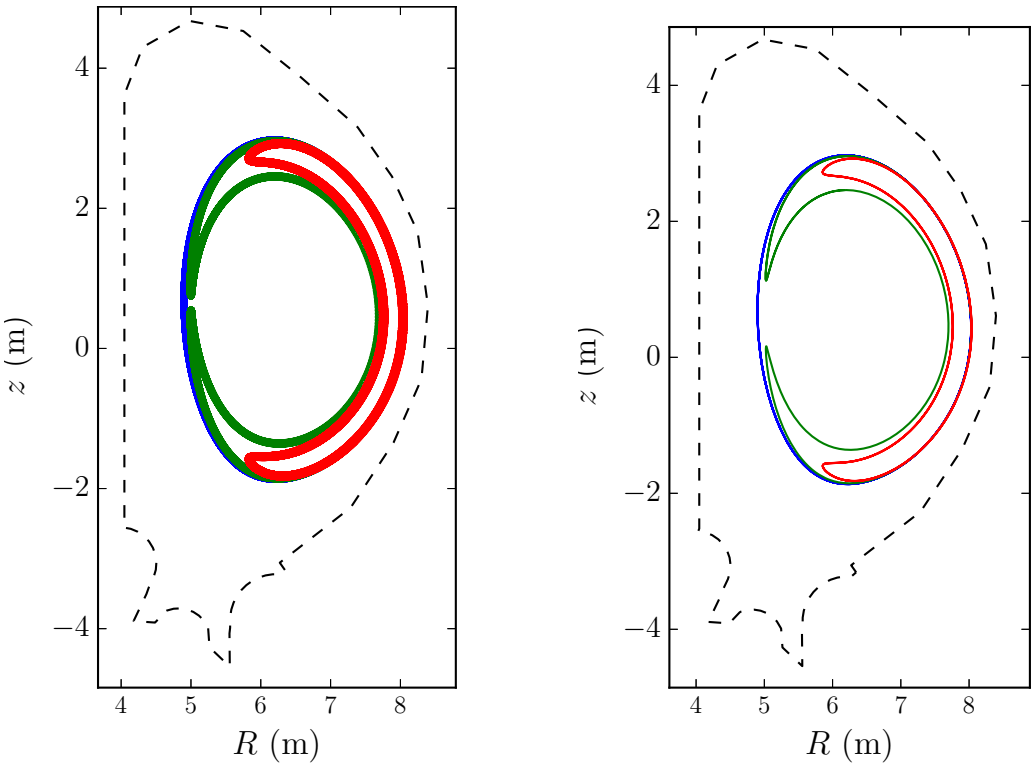


**(a)** Particle motion method **(b)** Guiding-center method

**Figure 13:** Three different particle orbits for an alpha particle simulated using both the particle motion method (a) and the guiding-center method (b). For each orbit, the particle was placed in $(R, z) = (8, 0)$ m and given a kinetic energy of 3.5 MeV. The values of $\xi_0$ were $\xi_0 = 0.5$ (red), $\xi_0 = 0.6$ (green) and $\xi_0 = 0.7$ (blue). As can be seen, the orbits simulated using the particle motion method comes closer to the transition point between the banana and passing orbit. This is expected, and due to properties of the guiding-center method.

center orbits, the $E_\perp$ term never attains the full energy of 3.5 MeV. The particle will therefore never have to stop, in contrast to the other orbits, but can continue moving along the magnetic field lines, thus forming a passing orbit.

Another thing worth noting is the quite large temporal offset between the energy components for the particle orbit resulting from $\xi_0 = 0.6$ and the energy components for the corresponding guiding-center orbit. As we will see later, this quite large offset appears for the same reasons as the corresponding particle orbit in Fig. 13a was elongated, compared to the guiding-center orbit resulting from $\xi_0 = 0.6$ in Fig. 13b. This offset in the energy however gives us a hint that just a small change in mirror point position will have significant effects on the orbit time (i.e. the time it takes for the particle to return to its initial position), when the mirror point is close to the transition point.

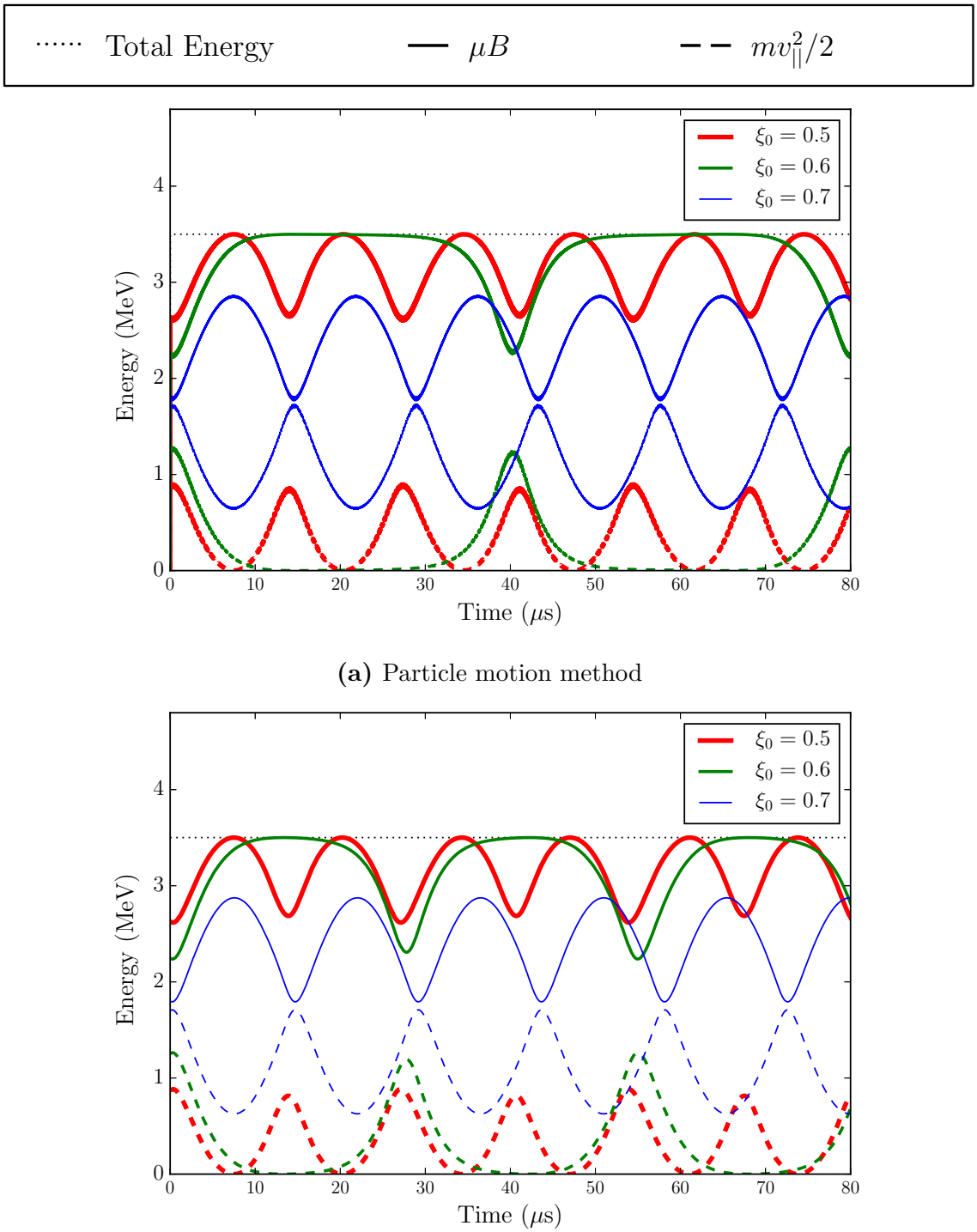


**(a)** Particle motion method

**(b)** Guiding-center method

**Figure 14:** The total energy (dotted lines), parallel energy ($E_{\parallel}$, dashed lines), and perpendicular energy ($E_{\perp}$, solid lines) components for the orbits of Fig. 13. The value of $\xi_0$ was varied between $\xi_0 = 0.5$, $\xi_0 = 0.6$ and $\xi_0 = 0.7$. It is particularly interesting to note how the $E_{\parallel}$ term goes to zero for the two banana orbits (red and green), while for the passing orbit $E_{\parallel} > 0$.

The successive transition into a passing orbit observed in Fig. 13 for increasing $\xi_0$ leads to the conclusion that there must be some value of $\xi_0$, let's call it $\xi_c$, that is such that for all $\xi_0 < \xi_c$ a banana orbit is formed, while for all $\xi_0 > \xi_c$ a passing

orbit is formed. In Fig. 15 this value has been plotted as a function of the radial distance to the center of the fusion device. When generating the figure, an electron with energy $E \approx 1.25\,\mathrm{keV}$ was placed in $z \approx 0.5\,\mathrm{m}$, which is approximately the $z$-coordinate of the magnetic axis as shown in Fig. 5a. Had the particle been perfectly aligned with the magnetic axis, a value of $\xi_\mathrm{c} = 0$ would have been expected for all radii on the "inner" side of the magnetic axis. The guiding-center method was used for generation, as the particle motion method would require prohibitively long computation time.

For each radial position there are two values of $\xi_\mathrm{c}$ that determine the kind of orbit topology, since if $\xi_\mathrm{c}$ is one transition value, so is $-\xi_\mathrm{c}$. Because of this, the dependence is symmetric around the $\xi_\mathrm{c} = 0$ line. We also see that the border of the region forms a parabola, suggesting $|\xi_\mathrm{c}| \propto (R - R_\mathrm{M})^{1/2}$, where $R_\mathrm{M}$ is the $R$ coordinate of the magnetic axis.

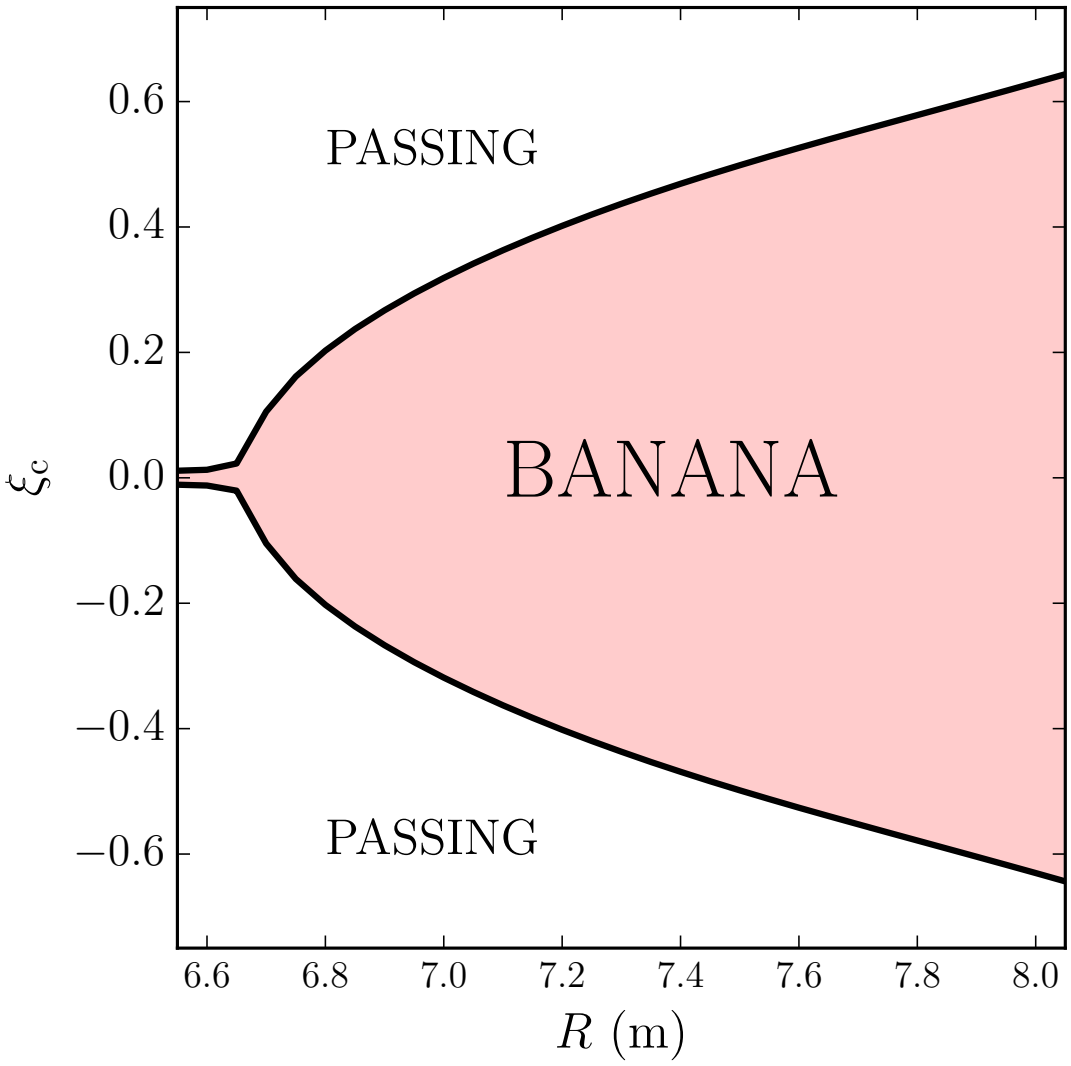


**Figure 15:** The ratio $\xi_\mathrm{c} = v_\parallel / v$ plotted as a function of $R$ with $z$ aligned with the magnetic axis. The particle used for simulations was an electron with energy $E \approx 1.25\,\mathrm{keV}$. When the particle's $\xi_0$ is within the enclosed region in the figure, a banana orbit will be formed. Otherwise, it will follow a passing orbit.

## 4.2 Explanation of orbits

In the previous section we observed some of the fundamental properties of the two most common orbit topologies found in tokamaks. Most of the observations made so far have yet to be explained; this is the purpose of this section. First we will try to use the theory derived in Sections 2.1.2 and 2.2.2 to explain the observed effects on the width of the banana orbits. Next, the banana width will be related to the orbit's deviation from magnetic field lines in order to explain the observations of Sections 4.1.1 and 4.1.2. Finally, the banana orbit's mirroring effect will be examined and an explanation for the observations will be given.

### 4.2.1 Effect of mass, charge and energy

After having seen that the banana width varies with both mass, charge and energy in Section 4.1.1, we would now like to understand what causes the banana width. The answer comes from the drifts derived in Sections 2.1.2 and 2.2.2. Note that the derivations made in those sections are merely two kinds of expressions for the same drifts.

Since drifts are perpendicular to the magnetic field lines, they will force the particle to move across field lines instead of just following them perfectly. The guiding-center velocity, as derived in Section 2.2.2, was found to be

$$\dot{\boldsymbol{X}} = v_{\parallel}\hat{\boldsymbol{b}} + \frac{m\hat{\boldsymbol{b}}}{qB^*_{\parallel}} \times \left( \frac{v_{\perp}^2}{2B}\nabla B + v_{\parallel}^2 \nabla_{\parallel}\hat{\boldsymbol{b}} \right). \tag{37}$$

In this expression we have a parallel velocity term, $v_{\parallel}\hat{\boldsymbol{b}}$, and a drift term. The charge sign dependence on the banana as observed in Fig. 9 then easily gets its explanation, as the sign of the charge determines the sign of the drift term. Depending on the charge sign, the guiding-center drift will be either to the left or right from the field line. Thus, for the positive charge sign of the proton, we saw how the guiding-center drifted towards the left side of the field line. For the protide on the other hand, the drift velocity would have been directed in the opposite direction, and thus it drifts off to the right of the field line.

Though the effect of the charge sign is easily seen from Eq. (37), the effect of mass, charge magnitude and energy is not as straight forward. In order to estimate the drifts we are now going to approximate the distance that the particle deviates from the field lines.

Since our fusion device is toroidally symmetric, Noether's theorem states that there is some corresponding conserved quantity. This happens to be the canonical angular momentum $p_\phi$, given by

$$p_\phi(R, z) = mRv_\phi + qRA_\phi, \tag{38}$$

where $R$ is the distance from the axis of symmetry of the device to the particle, $v_\phi$ the azimuthal component of the velocity and $A_\phi$ the azimuthal component of the magnetic vector potential. The poloidal magnetic flux between the magnetic axis and a given magnetic surface (also called flux surface) is $2\pi\Psi$, where the magnitude of $\Psi$ is

$$\Psi(R, z) = -RA_\phi(R, z).$$

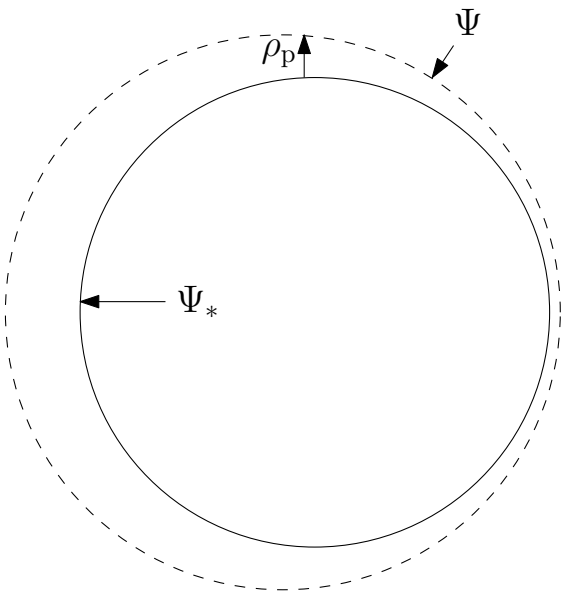


**Figure 16:** The definition of the poloidal Larmor radius, $\boldsymbol{\rho}_{\mathrm{p}}$, as the distance between an orbit and a magnetic surface, in terms of points on a given magnetic surface, and the particle's guiding-center orbit.

The canonical angular momentum (38) can then be written as

$$p_\phi(R, z) = mRv_\phi - q\Psi. \tag{39}$$

By definition, $\Psi$ is constant on a magnetic surface in an axially symmetric magnetic field, so the particle must drift across magnetic surfaces if $v_\phi \approx v_\parallel$ changes (which it does, as we have seen in Section 4.1.3). In other words, the *variation* of $\Psi$ and $v_\parallel$ must balance each other out.

We can introduce a quantity $\Psi_*$ defined as

$$\Psi_* = -\frac{p_\phi}{q}.$$

Combining this with Eq. (39) gives us

$$\Psi_* = \Psi - \frac{mRv_\phi}{q}. \tag{40}$$

This quantity $\Psi_*$, often referred to as the "drift surface", has a dimension of magnetic flux. For a given $p_\phi$, the magnetic surface for which the poloidal magnetic flux $\Psi$ is equal to $\Psi_*$ is the location of a particle with $v_\phi \approx v_\parallel = 0$. That is, at the mirror points (banana tips). This means that for a trapped particle the drift surface $\Psi_*$ is the magnetic surface that goes through the banana tips because there $v_\phi \approx v_\parallel$ vanishes. For a passing orbit $v_\parallel$ never vanishes, so the orbit never passes the drift surface, as illustrated in Fig. 16. This orbit is either always outside or inside the drift surface, depending on the sign of $q$.

As we established above in conjunction with Eq. (39), $\Psi$ must also vary if $v_\parallel$ varies. Here $\Psi$ does not label a specific flux surface, instead $\Psi(t)$ denotes the value of $\Psi$ along the particle trajectory.

We introduce a vector $\boldsymbol{\rho}_{\mathrm{p}}$ that is locally normal to the flux surfaces, and its length $\rho_{\mathrm{p}}$ is the distance between the particle location $\Psi$ and the drift surface $\Psi_*$, as is also

shown in Fig. 16. The magnitude of $\boldsymbol{\rho}_\mathrm{p}$ is

$$\rho_\mathrm{p} = \boldsymbol{\rho}_\mathrm{p} \cdot \frac{\nabla\Psi}{|\nabla\Psi|}, \tag{41}$$

and by construction

$$\boldsymbol{\rho}_\mathrm{p} \cdot \nabla\Psi = \Psi - \Psi_*.$$

The vector $\nabla\Psi$ is naturally normal to a flux surface. Using Eq. (40) we find

$$\boldsymbol{\rho}_\mathrm{p} \cdot \nabla\Psi = \frac{mRv_\phi}{q},$$

which combined with Eq. (41) gives

$$\rho_\mathrm{p} = \frac{mRv_\phi}{q|\nabla\Psi|}.$$

We can use that the poloidal magnetic field can be expressed as $\boldsymbol{B}_\mathrm{p} = \nabla\phi \times \nabla\Psi$, with $|\nabla\phi| = 1/R$ to find that $|\nabla\Psi| = RB_\mathrm{p}$. Thus

$$\rho_\mathrm{p} = \frac{mv_\phi}{qB_\mathrm{p}} \approx \frac{mv_\parallel}{qB_\mathrm{p}}.$$

This expression holds many similarities to that of the regular Larmor radius, $\rho$, as defined in Section 2.1, but this expression contains the poloidal field strength $B_\mathrm{p}$ and parallel velocity $v_\parallel$ unlike $\rho$. For this reason, we call $\rho_\mathrm{p}$ the *poloidal Larmor radius*. The poloidal Larmor radius is the typical distance a trapped particle moves away from the flux surface because of drifts.

We can estimate the orbit width $\delta$ from the variation of $\rho_\mathrm{p}$ along the orbit due to the variation of $v_\parallel$, denoted by $\Delta v_\parallel$:

$$\delta \approx \frac{m\Delta v_\parallel}{qB_\mathrm{p}}.$$

With this expression for the orbit width, we are able to estimate the effect of mass, charge magnitude and energy. Since $\Delta v_\parallel = \sqrt{2\Delta E_\parallel/m}$ we can write the orbit width as

$$\delta = \frac{\sqrt{m}}{q}\frac{\sqrt{2\Delta E_\parallel}}{B_\mathrm{p}}, \tag{42}$$

where the ratio $\sqrt{m}/q$ appears. It was something like this that was predicted in Sections 4.1.1 and 4.1.2, and when numbers are put in it also appears to agree with the simulations of Section 4.1.2 quite well. From Eq. (42) we calculate that the guiding-center orbit widths for $\mathrm{D}^+$ and $\mathrm{T}^+$ should be fairly similar, and differing only by a small amount. The widths for $\mathrm{C}^{6+}$ and especially $\mathrm{W}^{56+}$ on the other hand, should be much smaller. The width of the $\mathrm{C}^{6+}$ orbit compared to the orbit of $\mathrm{D}^+$ should differ by about 59 %, which is in good agreement with the simulation that gave the value as 57 %. For $\mathrm{W}^{56+}$ and $\mathrm{T}^+$, we estimate that the former's orbit should deviate by 86 % less than the latter's (simulated value was 85.3 %).

The observations made in Fig. 10 are also fairly well explained by Eq. (42). As we can see, the orbit width should be proportional to $(\Delta E_\parallel)^{1/2}$. This seems likely, since we can at least conclude that the width should be proportional to some power of $E$ between 0 and 1.

### 4.2.2 The mirroring effect

In Section 4.1.3, we saw how the parallel and perpendicular components of the guiding-center energy vary, which determines whether a banana or a passing orbit is followed. We also saw that in a banana orbit, the parallel velocity $v_\parallel$ goes to zero and is forced to change sign at the mirror points, forcing the particle to turn back. In this section we will elaborate on the reasons for the particle to follow a certain orbit, and relate the observations made in 4.1.3 to known mathematical theory.

Let us first recall the expression for the particle's energy,

$$E = E_\parallel + E_\perp = \frac{mv_\parallel^2}{2} + \mu B. \tag{43}$$

In Section 2.2.1, and especially Eq. (25), we learned that the magnetic moment $\mu = mv_\perp^2/2B$ is an adiabatic invariant, which means that $E_\perp$ should vary due to changes in the magnetic field strength. Looking at the magnetic field strength $B$ in Fig. 5b, we see that as the particle moves in the direction of decreasing $R$, the magnetic field strength $B$ increases, thus increasing $E_\perp$ along with it. Since the total energy must remain constant, $E_\parallel$ is therefore forced to decrease, which is consistent with the observations of Section 4.1.3. When the energy components vary, so must the speed components $v_\parallel$ and $v_\perp$. At a point with a sufficiently high magnetic field strength, the perpendicular energy term would completely dominate and force $E_\parallel$ to go to zero, bringing $v_\parallel$ to zero with it. At this point, which becomes the banana mirror point, it would not be possible for the particle to continue along its path into regions of even greater $B$, and so it is forced to go in some other direction. Since the orbit is approximately locked to a magnetic field line (only approximately since drifts will cause it to move across field lines) there is only one other possible direction in which the particle can go, i.e. the same way where it came from. Moving in that direction, combined with the drift effects described in Section 4.2.1, causes the orbit to look like a banana in the poloidal plane.

For certain values of $\xi_0$, the adiabatic invariant $\mu$ will be sufficiently small for $E_\perp$ never to dominate completely. In this case, $v_\parallel$ never goes to zero and is therefore never forced to change sign. The particle will just continue to follow a magnetic field line and form a passing orbit. This was the case for the orbit with $\xi_0 = 0.7$ in Fig. 14, where we could see how the $E_\perp$ term remained below 3.5 MeV at all times for this initial condition.

So how would we go about making the particle go further along the field line, effectively making the banana longer? The key is in balancing the two energy terms $E_\parallel$ and $E_\perp$ appropriately. Assuming the initial position of the particle to remain unchanged, the magnetic field would obviously not change if we change any other particle parameter. We can therefore make the parallel energy $E_\parallel$ "last longer" by increasing its initial value, thus allowing the particle to go further before losing all its parallel velocity. This is done simply by increasing the particle's initial velocity in the direction parallel to the magnetic field. Note however that increasing $E_\perp$ at the same time, by an equal amount, would cause no change to the banana length.

Now, let $E_0$ denote the total energy of the system (which will remain constant in time). We may then rewrite Eq. (43) as

$$E_\parallel = E_0 - \mu B.$$

For a banana orbit, as we have seen, the $E_\parallel$ term will vanish in the mirror points of the banana. If we let $B_{\max}$ be the maximum strength of the magnetic field along the magnetic field line that the particle follows, we find that the particle will follow a banana orbit only if

$$E_0 - \mu B_{\max} < 0.$$

Rewritten, this can be stated as requiring that $\mu > E_0/B_{\max}$, for the particle to follow a banana orbit. But if we let $B_{\min}$ be the minimum magnetic field strength the particle experiences along the orbit, and note that $\mu$ can be expressed in terms of $v_\perp$ and $B$ in this point, as $\mu = mv_\perp^2/2B_{\min}$, we can use the fact that $\mu$ is constant and that $v_\parallel = 0$ (implying $v_\perp = v$) in the mirror points to substitute $E_0$ for $mv^2/2$ and find the condition for the particle to follow a banana orbit

$$\left|\frac{v_\perp}{v}\right| > \sqrt{\frac{B_{\min}}{B_{\max}}}.$$

Now, using the fact that $v_\perp^2 = v^2 - v_\parallel^2$ and the definition of $\xi$ in (36), we may express a condition for the initial value of $\xi$,

$$|\xi_0| < \sqrt{1 - \frac{B_{\min}}{B_{\max}}}, \tag{44}$$

which will cause the particle to follow a banana orbit.

### 4.2.3 Mirror point dependence of $\xi$

As mentioned in Section 3.1, a simple approximation for the magnetic field strength is

$$B(R) \approx \frac{B_0 R_0}{R}, \tag{45}$$

where $B_0$ is the field strength at the arbitrary point $R_0$. Using (45) we can rewrite (44) to find an expression for the location of the mirror points of the banana orbit. We already concluded that the magnetic field strength attains its maximum value, $B_{\max}$, in the banana mirror points. If we call the radial position of the mirror point $R_{\max}$, Eq. (44) becomes an equality in this point. it now expresses the value of $\xi_0$ that gives a mirror point in $R = R_{\max}$. Here we can use the magnetic field approximation (45) to approximate both $B_{\min}$ and $B_{\max}$, and substituting these into (44) and solving for $R_{\max}$, we find

$$R_{\max} = \left(1 - \xi_0^2\right) R_{\min}. \tag{46}$$

For a particle starting with its $z$ coordinate aligned with the magnetic field axis, $R_{\min}$ becomes the initial $R$ of the particle. In Fig. 17, the mirror points for an alpha particle starting in $(R, z) = (7.9, 0.5)\,\mathrm{m}$ (almost aligned with the magnetic axis), plotted as a function of $\xi_0$ is shown. Simulation was done using the guiding-center method. The figure also includes the theoretical curve predicted from Eq. (46) with $R_{\min} = 7.9\,\mathrm{m}$, and as can be seen the simulated curve agrees quite well. The small deviation is most likely due to that the orbit is not initiated with $z$ exactly aligned with the magnetic axis.

This dependence is interesting as it gives us a very simple (yet apparently quite good) method for predicting whether a particle will follow a banana or a passing orbit, just from knowing its initial position (given $z$ is aligned with the magnetic

axis) and $\xi_0$. In addition to what has already been said, it can be noted that for certain values of $\xi_0$ and $R_{\text{min}}$, the predicted $R_{\text{max}}$ will never be reached, as it lies too close to the center of the device. This is the case for all passing orbits, as can be seen from Eq. (44).

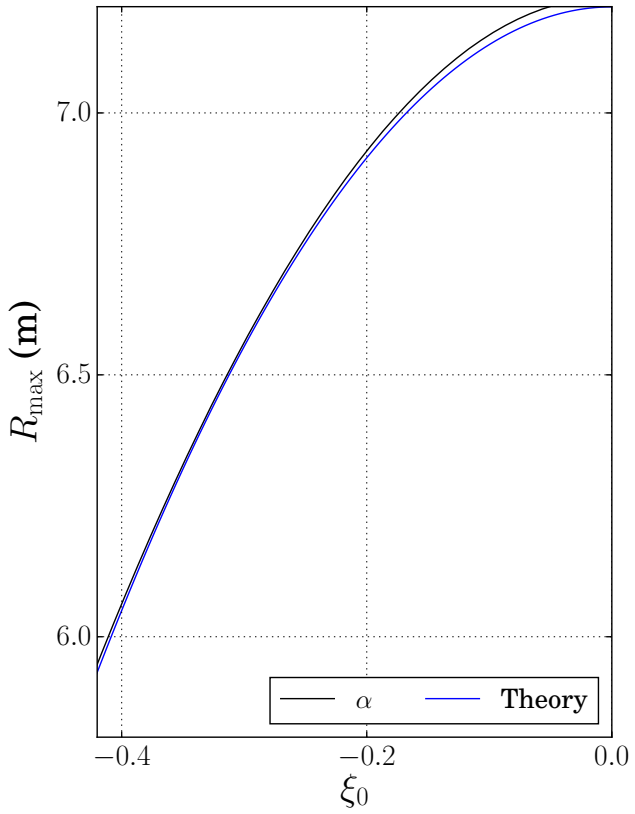


**Figure 17:** The mirror point as a function of initial $\xi$ for an alpha particle compared with the theoretical position given by $R_{\text{max}} = R_0(1 - \xi^2)$. The coordinates $(R_0, Z_0)$ for the initial position used in the simulation were $(7.9, 0.5)$ m.

In Eq. (44) we could, instead of just studying any mirror point, study the transition point $\xi_{\text{c}}$, which sets the limit for a banana and a passing orbit. The simulation results of its value for an electron, starting with $z$ aligned with the magnetic axis, was shown in Fig. 15. Here, we can start from Eq. (44) and note that for a banana orbit reaching just to the transition point, $R_{\text{c}}$, the maximum magnetic field strength is $B_{\text{max}} \approx B_0 R_0 / R_{\text{c}}$. Substituting this approximation, along with a similar approximation for $B_{\text{min}}$, we find

$$|\xi_{\text{c}}| = \sqrt{1 - \frac{B_{\text{min}}}{B_{\text{max}}}} = \sqrt{1 - \frac{R_{\text{c}}}{R_{\text{min}}}}. \tag{47}$$

This gives the value of $\xi_0$ that separates the banana orbits from the passing orbits. The transition values for $\xi_0(R)$, as given by (47), were shown in Fig. 15 and the estimated $R_{\text{min}}$ dependence for $\xi_{\text{c}} \propto (R_{\text{min}} - R_{\text{M}})^{1/2}$ given there appears to be approximately true. In Eq. (47), we also find support for the statement that $\xi_{\text{c}}$ should go to zero as $R_{\text{min}}$ approaches alignment with the magnetic axis in the $z$ direction.

Since magnetic field lines are similar to ellipses converging towards the same point, being perfectly aligned with the magnetic axis would allow the particle to start from $R_{\min} = R_{\mathrm{M}}$. As $R_{\min}$ goes to $R_{\mathrm{M}}$, so would $R_{\mathrm{c}}$. When $R_{\min} = R_{\mathrm{M}}$ finally, we would also have $R_{\mathrm{c}} = R_{\mathrm{M}}$ and so $\xi_{\mathrm{c}}$ would be zero.

Another interesting conclusion can be drawn from Eq. (47) regarding the mirror point location, as predicted by Eq. (46). By definition we will have a passing orbit for all values of $\xi_0 > \xi_{\mathrm{c}}$, but since the orbit is locked to a magnetic field line, it should still pass the transition point (neglecting drifts). The "mirror point" (which is rather a furthest point for the passing orbit) as predicted by Eq. (46) is no longer valid, and must therefore only apply to banana orbits. For passing orbits, the "mirror point" is instead approximately equal to the transition point $R_{\mathrm{c}}$. Due to the increased effect of particle drifts however, the orbit will in reality pass through a point $R < R_{\mathrm{c}}$.

## 4.3 Comparison between simulation methods

Previously we have introduced the guiding-center formalism, separating the small scale gyro-motion from the average motion of the particle, in which our main interest lies. In this way we have been able to simulate the motion of the particle throughout the device without needing to calculate the gyration at each point. However, up to this point we have not yet discussed the quality of this transformation regarding the physics and the resulting trajectory of the particle. In this section, we will compare the two equations with each other in terms of energy conservation, orbit topology and also computational time.

### 4.3.1 Energy Conservation

The first topic to be studied in this section will be the energy conservation as a function of time for both methods. The aim is to observe the difference between the methods concerning energy conservation for a fixed choice of initial parameters.

The energy conserving property of solutions for particle motion and guiding-center motion is compared in Fig. 18. The trajectories were simulated over a time period of 0.8 ms, with a fixed error tolerance $\varepsilon_0 = 10^{-7}$. It is clear from the plot that for the particle motion a numerical error accumulates, causing the energy to increase. The energy change in the guiding-center approach is not appreciable during the simulation time.

The simulations used to produce Fig. 18 bring other numerical advantages of the guiding-center motion into light. The particle simulation took 63.3 s to execute, producing 1 980 815 data points. Meanwhile, the guiding-center simulation execution time was 1.1 s and produced 4 474 data points. The amount of steps taken to produce the sizable number of data points for the particle motion is what causes the energy level to deviate, since the RKF45 method is not inherently energy conserving and thus causes the error to accumulate. The fact that the RKF45 method is the cause of this inaccuracy makes it possible to regulate the conservation of energy depending on method and initial parameters used. This will be utilized in the following section.

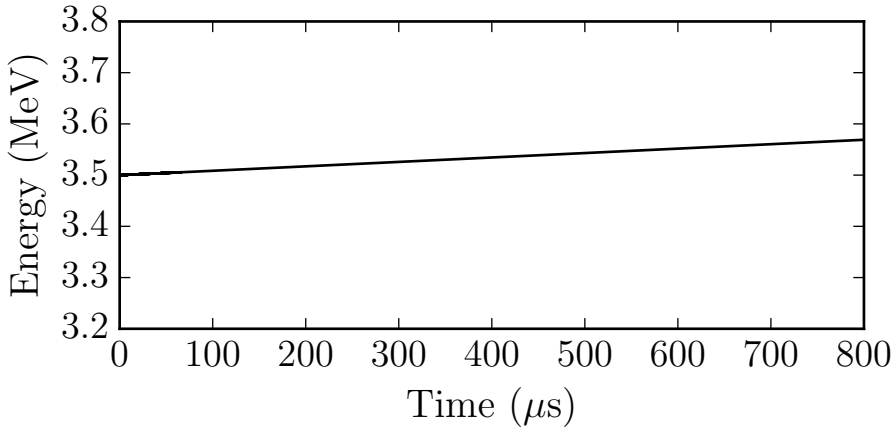


**(a)** Energy for particle motion. The energy is not conserved, it accumulates.

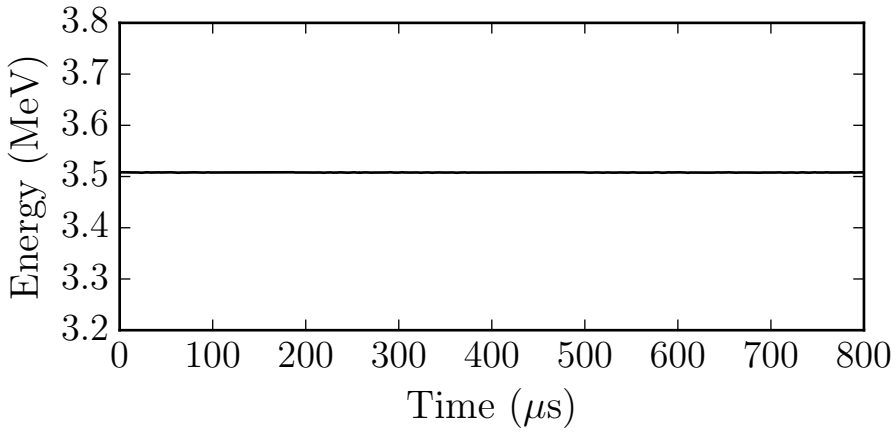


**(b)** Energy for guiding-center motion. The energy is seemingly conserved.

**Figure 18:** Energy for alpha particles plotted over time for the numerical solutions of the particle motion and guiding-center motion. All parameters were the same for both simulations.

### 4.3.2 Computational time

In this section we will study the program execution time for the two methods, as we increase the time for which we want to follow the particle. In this way, this section will give another motivation of the guiding-center method, as well as motivating the use of particles with higher energies, compared with the values expected in a thermal plasma.

If a comparison of the computational time between the methods is to be done correctly, it is important that both of the equations result in the same energy conservation. The amount of which the initial and final energy values deviate, will be regarded as a calibration parameter, putting both of the algorithms on equal ground.

As presented in Section 3.2, the optimal step size $h_{\text{opt}}$ is calculated with respect to the fixed error tolerance $\varepsilon_0$, see Eq. (34). The smaller the step size, the greater the accuracy in the result compared with the theoretical prediction. Hence, a smaller value of $\varepsilon_0$ will lead to a better conservation of energy. Since the number of steps taken differ greatly between the implementation of the guiding-center equations and the equations of particle motion, it follows that the latter is far more dependent on the step size and thus the error tolerance $\varepsilon_0$. In the comparison that

follows, we will fix the order of energy conservation to about six digits, so that $E_{\text{initial}}/E_{\text{final}} = 1 \pm 0.5 \cdot 10^{-6}$.

For a start, let us define the simulation length $t_{\text{end}}$ as the time for which the orbit should be traced. Likewise, we define the *wall-clock time* as the actual time it takes to run the program for a certain simulation. The wall-clock time taken for a particular method to calculate the needed data points, as a function of simulation length, is given by Fig. 19. There we see that the wall-clock time for the guiding-center method is much less, and increases slower, than for the corresponding particle motion algorithm.

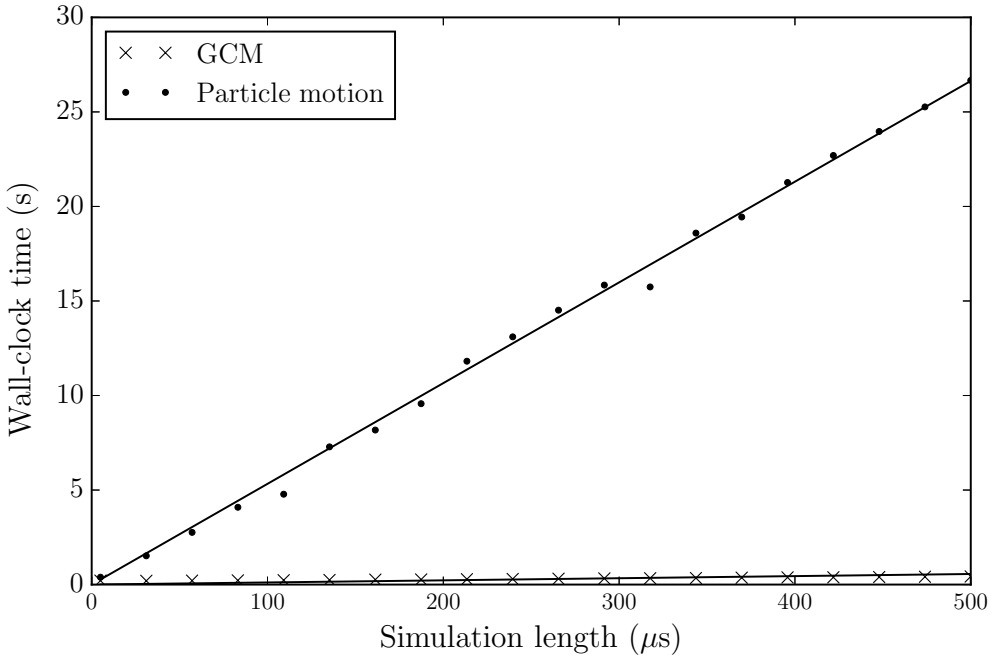


**Figure 19:** Comparison between the particle motion method and the guiding-center motion method of how much wall-clock time calculations require to complete. On the $x$ axis is the simulation length, i.e. $t_{\text{end}}$, and on the $y$ axis is the wall-clock time it took for the program to carry out the calculations. A linear curve fit has been made to the data which gives an inclination of $k_{\text{PM}} \approx 53\,300$ for particle motion and $k_{\text{GCM}} \approx 1\,100$ for guiding-center motion. That means the guiding-center method implemented is almost 50 times faster than the particle motion method.

One thing we notice when running simulations of particles with different energies, is that the wall-clock time increases with energy. The simulation time it takes for a low energy particle to travel a certain distance is higher than the simulation time it would take for a particle with higher energy to cover the same distance. As the simulation time increases, so does the number of data points calculated for this particular particle. Since there is a limit to how many data points we can store, this is something we must take into consideration.

To conclude the results, we see that if we want to study low energy particles or orbits during a long simulation time, the wall-clock time needed to perform the simulations will be quite long when using the particle motion method. This is however not necessarily the biggest concern, as the vast amount of data points generated also can pose a problem. For these reasons, to able to study how the two

methods perform when simulating the actual plasma particles, a higher energy will be used with the value of 1 MeV, compared to the 10 keV expected for a thermal plasma. Note that this does not affect the high energy alpha particles which will still have an energy of 3.5 MeV.

### 4.3.3 Particle trajectories

Now we wish to see if there exists any situation, or set of parameters, where the guiding-center position differs from the real particle position. In the previous sections, the trajectories calculated using both methods were presented and we saw that the orbits did not seem to deviate from each other. However, when studying the radial coordinate for the mirror point as a function of $\xi_0$ in Fig. 20, we see that there is a slight deviation.

In Figures 20c and 20d, we can make a couple of interesting observations. First, we note that the mirror points for the alpha particle seem to have the largest deviation between the two methods. The mirror points of the tritium particle also deviates somewhat, while both the carbon and deuterium particles are almost perfectly aligned for both methods. Looking at Figures 20a and 20b we can see that the overall discrepancies are rather small, but anyhow, it is of interest to see how these differences arise.

It seems appropriate to first remind ourselves of the differences between the guiding-center approximation and the equations of motion for the particle motion. In Section 2.2.1 we derived the guiding-center Lagrangian under the assumption that the Larmor radius is much smaller than the spatial scale of the magnetic field variation. This enabled the possibility to expand the field in a Taylor expansion around the guiding-center $\boldsymbol{X}$. As mentioned in Section 2.1.2, this condition is equivalent with the requirement that the Larmor radius obeys $\rho \ll L_{\mathrm{B}}$, where the characteristic length $L_{\mathrm{B}}$ was defined by $L_{\mathrm{B}} = B/|\nabla B|$.

With this in mind, a natural question appears: in what way will the mirror position change if the requirement $\rho \ll L_{\mathrm{B}}$, and hence the guiding-center approximation, fails? This question can be answered by going back to Section 4.2.3 and looking at the theory of the mirror mechanism and the derivation of the mirror point radial coordinate. The derivation done there was based on the fact that $\mu$ is constant, however this is true only when dealing with the guiding-center Lagrangian, as derived in Section 2.2.1. For the particle motion orbit, the magnetic moment is instead an adiabatic invariant, as mentioned in Section 2.2.1 and proven in Appendix C.

The consequence of this difference is that while the orbit calculated from the guiding-center equations of motion always has $\mu$ as an exact constant, the orbit calculated from the equations of particle motion does not. Therefore, if there is even a slight change in $\mu$, the latter orbit will be adjusted accordingly while the former will remain the same. This would make the orbits deviate from each other. This fact can be used to derive new mirror positions for each method. Assume that at the mirror point, the value of the magnetic moment has changed with a small constant $\epsilon$, $\mu = \mu_0 \pm \epsilon$, where $\mu_0$ is the value of the constant magnetic moment as seen by the guiding-center orbit. Therefore, while the guiding-center orbit will be reflected at the point $R_{\mathrm{max,gc}}$, given by turning Eq. (46) into the equality

$$R_{\mathrm{max,gc}} = (1 - \xi_0^2)R_0,$$

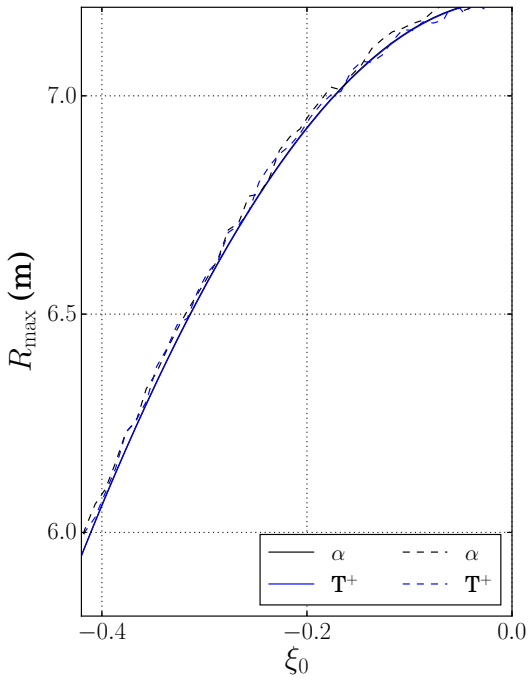


**(a)** Alpha and $T^+$ particles

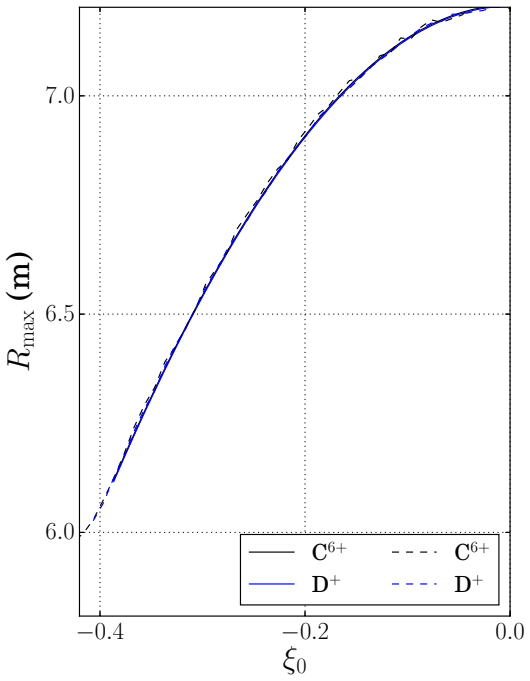


**(b)** $C^{6+}$ and $D^+$ particles

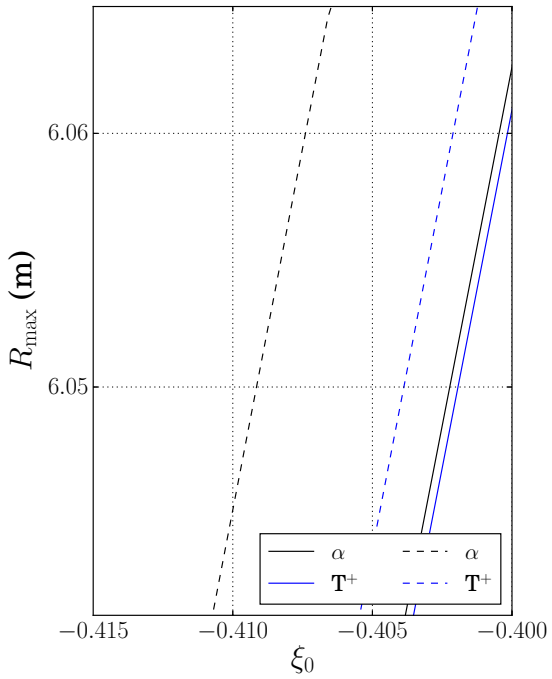


**(c)** Magnification: Alpha and $T^+$ particles

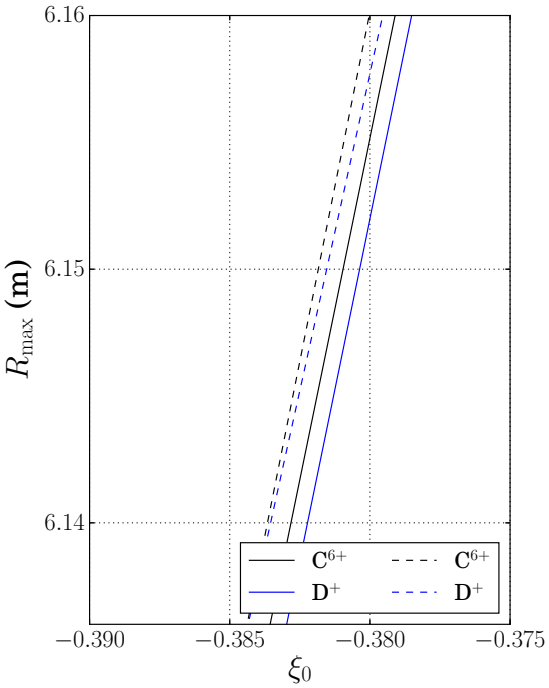


**(d)** Magnification: $C^{6+}$ and $D^+$ particles

**Figure 20:** The position of the guiding-center mirror points as a function of $\xi_0$ for different particles. The dotted lines are particle motion, the solid lines are guiding-center motion. The initial radial position was fixed at $R = 7.9\,\mathrm{m}$. The energies given were 1 MeV to the $D^+$, $T^+$ and $C^{6+}$ particles, while 3.5 MeV was given to the alpha particle.

the particle orbit will instead be reflected at a point

$$R_{\max,\mathrm{pm}} = (1 - \xi_0^2)R_0 \pm \Delta,$$

where $\Delta = \epsilon 2B_0R_0/mv^2$, which arises when we calculate the new mirror point from the added correction *epsilon* to $\mu_0$. Hence, we see that if the magnetic moment changes, we should be able to see a small deviation in the position of the mirror point for a particle simulated with the particle motion method, compared with the guiding-center method.

Furthermore, in Eq. (32) of Section 3.1 we found that the magnetic field was approximately inversely proportional to the major radius, $B \propto R^{-1}$. It then follows that $|\nabla B| \propto R^{-2}$. The length $L_\mathrm{B}$ is thus directly proportional to the radius, since $L_\mathrm{B} = B/|\nabla B| \propto R$. For smaller values of $L_\mathrm{B}$, corresponding to smaller values of $R$, it seems that the condition $\rho \ll L_\mathrm{B}$ would be less fulfilled, and we should see a greater deviation. This is verified by looking very closely at at Figures 20a and 20b, where the related curves are more separated for larger values of $|\xi_0|$ while they become more intertwined as $|\xi_0|$ decreases.

Next, let us see what happens if we increase the value of the Larmor radius $\rho$, which would (according to our deductions so far) lead to an increase in the deviation. The Larmor radius can, as we know by now, be written as $\rho = mv_\perp/qB$. For larger values of the ratio $m/q$, the Larmor radius should increase, and hence the deviation should be larger. In the earlier observations, we noticed that of tritium, deuterium and carbon, the tritium particle was the one with the greatest deviation between its particle and guiding-center mirror points. This is because of its large mass-to-charge ratio. However, for the alpha particle the mass-to-charge ratio is the same as for carbon and deuterium, though the mirror point deviation is the much larger. This leads us towards the next parameter affecting the inequality $\rho \ll L_\mathrm{B}$, namely the energy.

From Section 4.2.3, we know that at the mirror point we have $v_\parallel = 0$ which means that $E_0 = \mu B = mv_\perp^2/2$. This implies that $v_\perp = \sqrt{2E/m}$ at the mirror point. With the Larmor radius equal to $\rho = mv_\perp/qB$, we get $\rho = (m/qB)\sqrt{2E/m}$. Now, if we look at the guiding-center simulations done in Fig. 20 for the tritium and alpha particles respectively, we notice that the mirror point for the guiding-center does not seem to be affected at all. From this, it follows that, the point at which the guiding-center orbit is reflected is the same for both, which indicates that the magnitude of the magnetic field will be the same for both. If we let

$$\rho_\alpha = \frac{m_\alpha}{q_\alpha B}\sqrt{\frac{2E_\alpha}{m_\alpha}}, \qquad \rho_T = \frac{m_T}{q_T B}\sqrt{\frac{2E_T}{m_T}},$$

we get that

$$\frac{\rho_\alpha}{\rho_T} \approx 0.58\sqrt{\frac{E_\alpha}{E_T}},$$

and if we use the fact that $E_\alpha = 3.5E_T$ we get

$$\rho_\alpha \approx 1.09\rho_T,$$

at the mirror point. It seems that due to the higher energy, the Larmor radius for the alpha particle orbit has slightly increased compared with the Larmor radius for the

tritium particle orbit. This suggests that the difference between the guiding-center and the particle motion method for the alpha particle orbit should be slightly larger when compared to the corresponding distance for the tritium particle orbit, which is consistent with Fig. 20.

# 5 Summary and Discussion

We have now studied how different particles in a typical fusion plasma behave, and developed the necessary theory to explain our results. In this section we wish to discuss our findings regarding different orbit topologies, occurring in the magnetized plasma, and the importance of our results. In the end, we will draw the most important conclusions and show how the theory can be generalized for further investigation of more complex phenomena. We will begin by briefly summarizing the developed tools and theory, together with our main results.

Armed with the theory of charged particle motion in magnetic fields, and the guiding-center transformation, we developed a software tool in order to calculate particle and guiding-center orbits. A major component of this tool is the time-integration kernel. In addition, modules for interpolating the given magnetic field data, the check of whether the particle remained within the fusion device and for plotting the resulting orbits, were implemented. In order to have particle orbits that were realistic, magnetic field data from the ITER project was used.

Using the tool developed, our main observation is the existence of the different orbit topologies: *passing* and *trapped*. The latter is also called the *banana orbit*. It is found that this particular orbit has a varying width, caused by different drifts of the charged particle, and that it depends on the particle parameters. It is observed, and shown mathematically, that this width increases linearly with speed and by the square root of mass, while it is inversely proportional to the particle charge. Out of the typical plasma particles, we see that the alpha particle has the widest banana orbit, while the electron has a very thin orbit.

We realize the importance of the quantity $\xi_0 = v_\parallel/v$, where $v$ is the total speed of the particle, and $v_\parallel$ the speed along the magnetic field lines. This quantity proves to be valuable not only in determining the orbit topology, but also the length of the banana orbit. It is found that the shape of the magnetic field is the reason for the type of orbit, and an expression for the location of the mirror point is derived. Finally, we investigate the differences between the guiding-center and the particle following algorithms. The methods are compared in terms of time and energy conservation, both strongly motivating the use of the guiding-center method. By inspecting our ordering between the Larmor radius $\rho$ and the magnetic field scale length $L_\mathrm{B}$, we can conclude that if deviation between two orbits calculated using the guiding-center and particle motion methods, should occur, it would be at the mirror points. Despite the small energy differences, the expected deviation can be observed in the related simulations.

## Outlook

From the conclusions above, a first consequence is clear: alpha particles on wide banana orbits, too close to the boundary, will escape the confined region and collide with the wall of the device [20]. Apart from losing energy needed to sustain high plasma temperatures (as the alpha particles are very energetic), this may also cause damage to the device components. Knowledge of these losses is therefore crucial when designing a fusion device.

Apart from the risk of direct collisions with the wall, the confinement of the plasma is also greatly affected by the ongoing process of diffusion. Diffusion is the gradual transportation of particles and energy. This transport is caused by two

different kinds of collisions between particles. The first, called "classical" collisional transport, is the result of two particles colliding with each other, leading to a jump to an adjacent field line, about one Larmor radius away, either in the outward or inward direction. In the presence of a pressure gradient, the result is a gradual, slow diffusion of particles and heat towards the device wall. The rate of diffusion – how fast the particles move towards the wall – sets a limit on the confinement time of the plasma.

Because of the existence of trapped particles, we also have a transport due to so called "neoclassical processes". This is dominated by collisions between trapped particles, which are then deflected or displaced to other orbits. The size of this displacement is proportional to the banana width, and thus greater than the corresponding jump of the particles subject to the classical collisions. The wider the orbit, the bigger the displacement of the colliding particles, thus neoclassical processes lead to a higher rate of diffusive transport.

Another important effect present because of the different orbit topologies, is a naturally induced current in the plasma, named the *bootstrap current*. The bootstrap current is ultimately the result of the conservation of momentum, in collisions between trapped and passing electrons. Together with different particle densities, a net parallel flow of particles is introduced. These flows are proportional to the pressure gradient in the plasma, and sums up to create the bootstrap current. To understand the importance of this result, we should look at the tokamak design.

In a tokamak, the confinement of the plasma is achieved by a purposefully shaped magnetic field, composed by two main parts. The poloidal component of the field is generated by a plasma current that is induced by a transformer. The bootstrap current is flowing in the same direction as the one induced by the transformers. Therefore, by using this naturally generated current, the current generated from the transformer can be reduced, making the tokamak more economically sustainable [21].

With the results summed up, a natural question arises: what should be done next? Well first, we should mention that while our results are based on a tokamak geometry, most of our findings apply in other magnetic configurations as well.

The developed theory can be generalized, for example, to the case of time-dependent magnetic and electric fields. This would result in the addition of other drifts, which would affect the orbit topologies accordingly. In order to take these effects into account, the theory derived for this project must be slightly altered, as must the simulation tool that was developed. Thanks to the modularity of the tool however, only minor modifications according to the new equations of motion would be needed.

Additionally, the effect of collisions could be included and hence the theory of the collisional transport developed.

In summation, we have now seen how even a basic model can demonstrate and explain important properties of the plasma used in the tokamak devices. With the developed tools the field of plasma physics has been introduced, and with some modification, can be used for even further investigations and understanding of this particular field of physics.

# References


[1] C. Nordling and J. Österman, *Physics Handbook*, 8th ed. Lund, Sweden: Studentlitteratur, 2011, ISBN: 978-91-44-04453-8.

[2] J. Wesson, The science of JET, *European Fusion p Development Agreement March* 2000, 2000.

[3] J. Wesson and D. J. Campbell, *Tokamaks*, English. Oxford: Clarendon Press, 2004, vol. 118, ISBN: 0198509227.

[4] L. Spitzer, The stellarator concept, *Physics of Fluids (1958-1988)* vol. **1**, no. 4 1958, 253–264, 1958.

[5] R. J. Goldston and P. H. Rutherford, *Introduction to Plasma Physics*. Bristol: Institute of Physics, 1995, ISBN: 0-7503-0325-5.

[6] F. F. Chen, *Introduction to Plasma Physics and Controlled Fusion, Plasma Physics*, English, 2nd ed. Boston, MA: Springer US, 1984, vol. 1, ISBN: 9781475755954.

[7] J. R. Cary and A. J. Brizard, Hamiltonian theory of guiding-center motion, *Rev. Mod. Phys.* vol. **81** 2 May 2009, 693–738, 2 May 2009. DOI: 10.1103/RevModPhys.81.693. [Online]. Available: http://link.aps.org/doi/10.1103/RevModPhys.81.693.

[8] R. G. Littlejohn, Variational principles of guiding centre motion, *Journal of Plasma Physics* vol. **29** 01 Feb. 1983, 111–125, 01 Feb. 1983, ISSN: 1469-7807. DOI: 10.1017/S002237780000060X. [Online]. Available: http://journals.cambridge.org/article_S002237780000060X.

[9] H. Goldstein, C. Poole, and J. Safko, *Classical Mechanics*, 3rd ed. San Francisco: Addison-Wesley, 2002.

[10] T. G. Northrop, *The adiabatic motion of charged particles*. John Wiley & Sons, Inc., 1963. [Online]. Available: http://hdl.handle.net/2027/mdp.39015048204716.

[11] V. D. Shafranov, Equilibrium of a toroidal plasma in a magnetic field, English, *Journal of Nuclear Energy.Part C, Plasma Physics, Accelerators, Thermonuclear Research* vol. **5**, no. 4 1963, 251–258, 1963.

[12] J. D. Hunter, Matplotlib: A 2d graphics environment, *Computing In Science & Engineering* vol. **9**, no. 3 2007, 90–95, 2007.

[13] D. K. Cheng, *Field and Wave Electromagnetics*, 2nd ed. Harlow, UK: Pearson Education Limited, 2014, ISBN: 978-1-29202-656-5.

[14] A. S. Ackleh, E. J. Allen, R. B. Kearfott, and P. Seshaiyer, *Classical and Modern Numerical Analysis : Theory, Methods and Practice*, English. Hoboken: CRC Press, 2009, ch. 7, ISBN: 1420091573.

[15] W. H. Press, S. A. Teukolsky, W. T. Vetterling, and B. P. Flannery, *Numerical Recipes in C (2Nd Ed.): The Art of Scientific Computing*. New York, NY, USA: Cambridge University Press, 1992, ISBN: 0-521-43108-5.

[16] Z. Hou, B. Lisena, M. Pireddu, and F. Zanolin, *Lotka-Volterra and Related Systems*, English. de Gruyter, 2013, ISBN: 9783110269857.

[17] A. Lamothe, *Tricks of the Windows Game Programming Gurus, Fundamentals of 2D and 3D game programming*. Indianapolis, Indiana: Sams, 1999, ch. 8, pp. 413–418. [Online]. Available: http://portal.aauj.edu/portal_resources/downloads/programming/windows_game_programming_guru.pdf.

[18] D. Zaslavsky and T. Beutlich, *Interp2d*, Dec. 17, 2014. [Online]. Available: https://github.com/diazona/interp2d.

[19] R. Budny, Fusion alpha parameters in tokamaks with high dt fusion rates, *Nuclear fusion* vol. **42**, no. 12 2002, 1383, 2002.

[20] D. S. Darrow *et al.*, Alpha particle losses from tokamak fusion test reactor deuterium–tritium plasmas, *Physics of Plasmas* vol. **3**, no. 5 1996, 1875–1880, 1996. DOI: 10.1063/1.871983. [Online]. Available: http://scitation.aip.org/content/aip/journal/pop/3/5/10.1063/1.871983.

[21] I. Pusztai, *Turbulent and neoclassical transport in tokamak plasmas*, ser. Doktorsavhandlingar vid Chalmers tekniska högskola. Ny serie, no: 3262. Department of Applied Physics, Nuclear Engineering, Chalmers University of Technology, 2011, ISBN: 978-91-7385-581-5.

[22] H. J. de Blank, Guiding center motion, [Online]. Available: http://iter.rma.ac.be/Stufftodownload/Texts/GuidingCenterMotion.pdf.

# A Derivation of the charged particle Lagrangian

Before beginning with the derivation we remind that the usual expression of a Lagrangian is of the form $L = T - V$ where $T$ is kinetic energy and $V$ is potential energy. However, this only applies when the potential $V$ is independent of the velocity $\dot{q}_i$, were $q_i$ is the $i$-th component of the generalized coordinates. Nonetheless, the Lagrangian formalism can be generalized to velocity dependent potentials if the generalized force $Q_i$ satisfies the equation

$$Q_i = \frac{d}{dt}\Big(\frac{\partial U}{\partial \dot{x}_i}\Big) - \frac{\partial U}{\partial x_i}, \tag{48}$$

for a velocity dependent potential $U(q, \dot{q}, t)$. The Lagrangian can then be written as $L(q, \dot{q}, t) = T(q, \dot{q}, t) - U(q, \dot{q}, t)$. This will be useful in the following derivation.

A charged particle in an electromagnetic field experiences the Lorentz force as seen in Eq. (1). It is clear that the force depends on the velocity and thus the formalism extended to include velocity dependent potentials needs to be used. Our goal now is to express the generalized force of the system according to (48). First we choose our generalized coordinates to be the regular Cartesian coordinates $x, y, z$ since there are no constraints. For simplicity, we now use index notation. The Lorentz force (1) in index notation is

$$F_i = q(E_i + \epsilon_{ijk} v_j B_k), \tag{49}$$

where $\epsilon_{ijk}$ is the three dimensional Levi-Civita symbol. Note that this $q$ denotes the particle charge and has nothing to do with the coordinates $q_i$. By introducing the vector potential $\boldsymbol{A}(\boldsymbol{r}, t)$ and the scalar potential $\phi$ we have the following identities:

$$E_i = -\partial_i \phi - \partial_t A_i, \quad B_k = \epsilon_{klm} \partial_l A_m.$$

We start by calculating $\epsilon_{ijk} v_j B_k$ from the Lorentz force (49):

$$\begin{aligned} \epsilon_{ijk} v_j B_k &= \epsilon_{ijk} v_j \epsilon_{klm} \partial_l A_m = \big\{\epsilon_{ijk}\epsilon_{klm} = \delta_{mj}\delta_{li} - \delta_{mi}\delta_{lj}\big\} = \\ &= \delta_{mj}\delta_{li} v_j \partial_l A_m - \delta_{mi}\delta_{lj} v_j \partial_l A_m = v_j \partial_i A_j - v_j \partial_j A_i. \end{aligned}$$

Now insert this and the identity for $E_i$ into Eq. (49). Note that since $v$ has no explicit dependence on either $x, y$ or $z$, the product law gives $v_j \partial_i A_j = \partial_i v_j A_j$. We get

$$\begin{aligned} F_i &= q(-\partial_i \phi - \partial_t A_i + v_j \partial_i A_j - v_j \partial_j A_i) = \\ &= e[\partial_i (v_j A_j - \phi) - (\partial_t A_i + v_j \partial_j A_i)]. \end{aligned}$$

Examine the second term of this equation. Rewriting the second term as a total derivative will allow for simplifications:

$$\partial_t A_i + v_j \partial_j A_i = \frac{\partial A_i}{\partial t} + \frac{\partial x_j}{\partial t}\frac{\partial A_i}{\partial x_j} = \frac{\mathrm{d}A_i}{\mathrm{d}t}.$$

Insert this into the expression for the Lorentz force above and we have

$$F_i = q\left(\partial_i (v_j A_j - \phi) - \frac{\mathrm{d}A_i}{\mathrm{d}t}\right) = \frac{\mathrm{d}}{\mathrm{d}t}(-qA_i) - \frac{\partial}{\partial x_i}\underbrace{(q\phi - q v_j A_j)}_{U}.$$

If we set $U = q\phi - qv_j A_j$ we have

$$\frac{\partial U}{\partial \dot{x}_j} = \frac{\partial U}{\partial v_j} = -qA_j.$$

Now let $j \mapsto i$. Finally we have the Lorentz force as

$$F_i = \frac{\mathrm{d}}{\mathrm{d}t}\frac{\partial U}{\partial \dot{x}_i} - \frac{\partial U}{\partial x_i},$$

which is of the form of Eq. (48). Thus we can conclude that the Lagrangian is given by

$$L = T - U = \frac{1}{2}m\boldsymbol{v}^2 - q\phi + q\boldsymbol{v}\cdot\boldsymbol{A}.$$

# B Gauge invariance of the Lagrangian

The phase-space Lagrangian is

$$L(\boldsymbol{q}, \boldsymbol{p}, \dot{\boldsymbol{q}}, \dot{\boldsymbol{p}}, t) = \boldsymbol{p} \cdot \dot{\boldsymbol{q}} - H(\boldsymbol{q}, \boldsymbol{p}, t), \tag{50}$$

where $\boldsymbol{p}$ is a $N$-dimensional generalized momentum and $\boldsymbol{r}$ is the corresponding generalized coordinate and $H$ is the Hamiltonian. The coordinates $(\boldsymbol{q}, \boldsymbol{p})$ may be transformed to any $2N$ coordinates $z^\alpha$ that parametrize the phase space. The functions $q^i(\boldsymbol{z}, t)$ and $p^i(\boldsymbol{z}, t)$ define the new parametrization. The total derivatives of the $\boldsymbol{q}$ coordinates become

$$\dot{q}^i = \frac{\partial q^i}{\partial t} + \frac{\partial q^i}{\partial z^\alpha}\, \dot{z}^\alpha. \tag{51}$$

Insertion of Eq. (51) into Eq. (50) yields a general form for the Lagrangian:

$$L = \Lambda_\alpha \dot{z}^\alpha - \mathcal{H},$$

where

$$\Lambda_\alpha = \boldsymbol{p} \cdot \frac{\partial \boldsymbol{q}}{\partial z^\alpha} \quad \text{and} \quad \mathcal{H} = H - \boldsymbol{p} \cdot \frac{\partial \boldsymbol{q}}{\partial t}\,. \tag{52}$$

Application of the phase-space Euler-Lagrange equations

$$\frac{\mathrm{d}}{\mathrm{d}t} \frac{\partial L}{\partial \dot{z^\alpha}} - \frac{\mathrm{d}L}{\mathrm{d}z^\alpha} = 0,$$

and rearrangement of terms gives the equations of motion

$$\omega_{\alpha\beta} \frac{\mathrm{d}z^\beta}{\mathrm{d}t} = \frac{\partial \mathcal{H}}{\partial z^\alpha} + \frac{\partial \Lambda_\alpha}{\partial t}\,, \tag{53}$$

where

$$\omega_{\alpha\beta} = \frac{\partial \Lambda_\beta}{\partial z^\alpha} - \frac{\partial \Lambda_\alpha}{\partial z^\beta}\,. \tag{54}$$

The addition of a total time derivative to the Lagrangian (52) does not change the equations of motion. We divide the derivative into two parts:

$$L \to L + \frac{\mathrm{d}F}{\mathrm{d}t} \iff \Lambda_\alpha \to \Lambda_\alpha + \frac{\partial F}{\partial z^\alpha}\,, \quad \mathcal{H} \to \mathcal{H} - \frac{\partial F}{\partial t}\,,$$

this is a gauge transformation. First we show the invariance of the right hand side of Eq. (53):

$$\frac{\partial \mathcal{H}}{\partial z^\alpha} + \frac{\partial \Lambda_\alpha}{\partial t} \to \frac{\partial \mathcal{H}}{\partial z^\alpha} - \frac{\partial^2 F}{\partial z^\alpha \partial t} + \frac{\partial \Lambda_\alpha}{\partial t} + \frac{\partial^2 F}{\partial t \partial z^\alpha} = \frac{\partial \mathcal{H}}{\partial z^\alpha} + \frac{\partial \Lambda_\alpha}{\partial t}\,.$$

Because the second partial derivatives commutate, the expression is invariant under the gauge transformation. For the left hand side, it is sufficient to show that $\omega_{\alpha\beta}$ is invariant. From the definition of $\omega_{\alpha\beta}$ in Eq. (54) it is obvious that it is invariant as a result of second partial derivatives commutating. We can thus conclude that the Lagrangian is gauge invariant.

# C Magnetic moment: an adiabatic invariant

When a system performs a periodic motion, the integral

$$I = \oint \boldsymbol{p} \cdot \mathrm{d}\boldsymbol{r},$$

taken over one period is a constant of motion. The integral $I$ is called a *Poincaré invariant*. The vector $\boldsymbol{p}$ is a generalized momentum and $\boldsymbol{r}$ is the corresponding generalized coordinate. Now assume that the system changes slowly compared to the gyroperiod. If the motion is almost periodic, as it is in our case, the integral $I$ is approximately constant and is called an *adiabatic invariant* [22]. More precisely, $I$ being a constant is an exponentially accurate approximation. That is, if the gyrofrequency is $\Omega$ and the time rate of changes in the system experienced by the particle is $\omega$, then it is a good approximation to any order in $\omega/\Omega$.

Let $\boldsymbol{X}$ denote the guiding-center position of the particle and $\boldsymbol{\rho}$ the gyration vector, centered at $\boldsymbol{X}$. The particle position is then the sum of these parts, $\boldsymbol{x} = \boldsymbol{X} + \boldsymbol{\rho}$. By only considering the velocity $\boldsymbol{v}_\perp$, which is perpendicular to the guiding-center velocity $\dot{\boldsymbol{X}}$, the generalized momentum is

$$\frac{\partial \mathrm{L}}{\partial \boldsymbol{v}} = \boldsymbol{p} = m\boldsymbol{v}_\perp + q\boldsymbol{A}.$$

Insert this into the integral $I$:

$$I = \oint (m\boldsymbol{v}_\perp + e\boldsymbol{A}) \cdot \mathrm{d}\boldsymbol{r} = I_1 + I_2. \tag{55}$$

The first term $I_1$ can be evaluated by parametrization. With $\Omega = \dfrac{qB}{m}$ being the gyration angular frequency we have

$$I_1 = \oint m\boldsymbol{v}_\perp \cdot \mathrm{d}\boldsymbol{r} = \left\{ \zeta = \Omega t, \boldsymbol{r} = \boldsymbol{\rho}(\zeta) \implies \mathrm{d}\boldsymbol{r} = \frac{\boldsymbol{v}_\perp}{\Omega}\,\mathrm{d}\zeta \right\} = \frac{m|\boldsymbol{v}_\perp|^2}{\Omega} \oint \mathrm{d}\zeta =$$
$$= 2\pi \frac{m v_\perp^2}{\Omega},$$

under the assumption that the perpendicular velocity $\boldsymbol{v}_\perp$ is independent of the gyration coordinate $\zeta$. The second term in Eq. (55) can be evaluated by applying Stokes theorem. With the relationship $\boldsymbol{B} = \nabla \times \boldsymbol{A}$ we get the surface integral

$$I_2 = \oint_{\partial S} q\boldsymbol{A} \cdot \mathrm{d}\boldsymbol{r} = \int_S q\boldsymbol{B} \cdot \mathrm{d}\boldsymbol{S}.$$

The surface $S$ is the area encompassed by the gyration orbit of $\boldsymbol{\rho}$. Now if the field varies slowly around the guiding-center position, we can expand the magnetic field by Taylor approximation around the guiding-center position $\boldsymbol{X}$

$$I_2 = \int_S q\boldsymbol{B}(\boldsymbol{x}) \cdot \mathrm{d}\boldsymbol{S} = q \int_S [\boldsymbol{B}(\boldsymbol{X}) + \boldsymbol{\rho} \cdot \nabla \boldsymbol{B}(\boldsymbol{X}) + \mathcal{O}(\rho^2)] \cdot \mathrm{d}\boldsymbol{S} = -\pi q \rho^2 B,$$

when dropping terms higher than $\mathcal{O}(\rho^2)$. The sign comes from the negative orientation of surface enclosed by the gyration motion. Using $\rho = v_\perp/\Omega$ and $\Omega = qB/m$ as

defined in Section (2.1.1), we get $I_2 = -\pi m v_\perp^2/\Omega$. Combining $I_1$ and $I_2$ and using $\mu = m v_\perp^2/2B$ we have the result

$$I = I_1 + I_2 = \frac{\pi m v_\perp^2}{\Omega} = \left\{ \Omega = \frac{q v_\perp^2}{2\mu} \right\} = 2\pi \frac{m}{q} \mu.$$

This demonstrates that $\mu$ is an adiabatic invariant.

# D Running the program

In order to run the `ode-solver` program, which is used for calculating particle orbits, a number of parameters must be specified. The parameters can be specified in two different ways, either directly on the command line or through a text file (called a `pi` file for "particle information"). Parameters can be specified from both sources, but parameters given in the input text file have precedence over parameters specified on the command line.

All numbers given to the program must consist of a series of decimal digits, optionally preceded by a sign (+ and −) and optionally containing a decimal point. The number may also be followed by an `e` or `E` character in turn followed by and optional sign and a decimal integer.

Note that by default, the ODE solver will solve the guiding-center equations of motion, as derived in Section 2.2.1. A special command given below, must be passed to the program in order to solve the particle equations of motion.

## D.1 Downloading and compiling

The ODE solver program has been made available open source and for free via GitHub (`https://github.com/eerosdisciples/ode-solver`). Therefore, the source code can be easily downloaded to your computer using the free version control system `git` (`http://git-scm.com/`), available on most platforms. To clone the `solver` repository using `git`, open a terminal (or equivalent) and type

```
$ git clone https://github.com/eerosdisciples/ode-solver.git
```

This will create a new directory called `ode-solver` in your current directory.

The ODE solver program has been written in the C programming language and is designed to be compiled with the GNU C Compiler. Due however to the high portability of C, it should be possible to compile using any other C compiler respecting the C99 standard.

The program has been tested on computers running Linux and Mac OS X computers, and has been found to both compile and run well. Though not tested, it should be possible to compile and run the program on any other POSIX system or Windows. Please note however, that the compilation routines outlined here may not be applicable to your system in these cases.

In order to compile the program after cloning it using `git`, step into the main directory (generally called `ode-solver`) and type

```
$ make
```

This will require the GNU build system, or equivalent, to be installed on your computer. The `make` command will initiate the compilation routine which will compile all files and link them into the `solver` executable.

## D.2 Command line arguments

The table below lists all the commands that can be passed to the program. These arguments are passed from the command line, but may be overriden by commands given in a `pi` file.

| Short argument | Long argument | Description |
|---|---|---|
| `-c` | `--particle-charge` *number* | Specify the particle charge in units of the elementary charge $e$. |
| `-d` | `--domain-file` *path* | Set the path to the file containing the domain. |
| `-f` | `--B-field-file` *path* | Set the path to the file containing the magnetic field data, with units of Tesla. |
| `-m` | `--particle-mass` *number* | Specify the particle mass in unified atomic mass units (u). |
| `-n` | `--no-guiding-center` | Trace the orbit of the particle, and not it's guiding-center. |
| `-o` | `--output-file` *path* | Specify the name of the output file containing the calculated data. |
| `-p` | `--print-settings` | Print the values of the parameters used at the top of the output file. |
| `-r` | `--r0` *x,y,z* | Set the initial position of the particle. $x$, $y$ and $z$ are numbers. |
| | `--t0` *number* | Specify the starting time. This is just an offset and has no physical implications. Given in seconds. |
| `-t` | `--tend` *number* | Set the final time in seconds. |
| `-v` | `--v0` $v_x$,$v_y$,$v_z$ | Set initial velocity of the particle in meters per second. $v_x$, $v_y$ and $v_z$ are numbers. |

Example command:

```
$ ./solver -c 2 -d data/iter.wall_2d -f data/iter2d.bkg -m
  4 -o output.csv -r 8.0287,-0.0105,0.2538 -t 3.2e-5 -v
  -9.5487e6,-7.7664e6,-4.1652e6
```

## D.3 Parameters from file

In order to load simulation parameters from a text file, simply provide the name of the text file as a command-line argument to the program. A parameter text file can be provided in conjunction with parameters passed on the command-line, but remember that parameters passed in the file hold precedence over parameters passed directly on the command-line.

In each line of the parameter file one parameter may be set. There are two kinds of parameters, value parameters (which are of the form `parameter=value`) and flags (which are trailed by an exclamation mark (!)). A full list of parameters and flags that may be specified in a parameter file is presented in the table below.

| Parameter | Description |
|---|---|
| `charge` | Specify the particle charge in units of $e$ |
| `domain_file` | Set the full, or relative, path to the file containing the domain data for the simulation |
| `magnetic_field` | Set the path to the file containing the magnetic field data |
| `mass` | Specify the particle mass in unified atomic mass units (u) |
| `no_guiding_center!` | Flag specifying that the particle orbit should be traced, not the guiding-center orbit |
| `output_file` | Set the path to the file to which the program output should be written |
| `print_settings!` | Flag specifying that all parameters used in the simulation should be written to the top of the output file |
| `r0` | Set the initial position of the particle as r0=$x_0, y_0, z_0$ |
| `t0` | Set the starting time of the simulation. This is just a time offset which has no physical implications |
| `tend` | Set the final time of the simulation |
| `v0` | Set the initial velocity of the particle as v0=$v_{x0}, v_{y0}, v_{z0}$ |

## D.4 Output data format

As indicated in the flow chart in Section 3.4, the output is written to a file with the file format comma-separated values (CSV). If the `print-settings!` flag was given in the `pi` file, or if the `-p` was passed to the program, there will be 8 header lines at the beginning of the file. The input parameters are displayed in the top six lines, trailed by a blank line and finally by the names given to the variables calculated. The data is presented as a comma-separated matrix, with each variable as a column vector. The output data from particle and guiding-center calculations are shown in Tables 3 and 4 respectively.

**Table 3:** Output from particle calculation.

| Parameters | Description |
|---|---|
| `T` | Simulation time (s) |
| `x, y, z` | Particle coordinates in a Cartesian coordinate system (m) |
| `vx, vy, vz` | Particle velocity in the $x$, $y$ and $z$ Cartesian direcions respectively (m/s) |
| `Energy` | Particle energy (eV) |
| `Epar` | Parallel energy component $E_\parallel$ (eV) |
| `Eperp` | Perpendicular energy component $E_\perp$ (eV) |

**Table 4:** Output from guiding-center calculation.

| **Parameters** | **Description** |
|---|---|
| `T` | Simulation time (s) |
| `u` | Parallel velocity, $v_\parallel$ (m/s) |
| `X, Y, Z` | Guiding-center coordinates, Cartesian (m) |
| `mu` | Magnetic moment $\mu$, (J/T) |
| `Energy` | Total guiding-center energy (eV) |
| `Xi` | $\xi = v_\parallel / v$ |
| `Ekin` | Particle kinetic energy (eV) |
| `muB` | Particle potential energy (eV) |